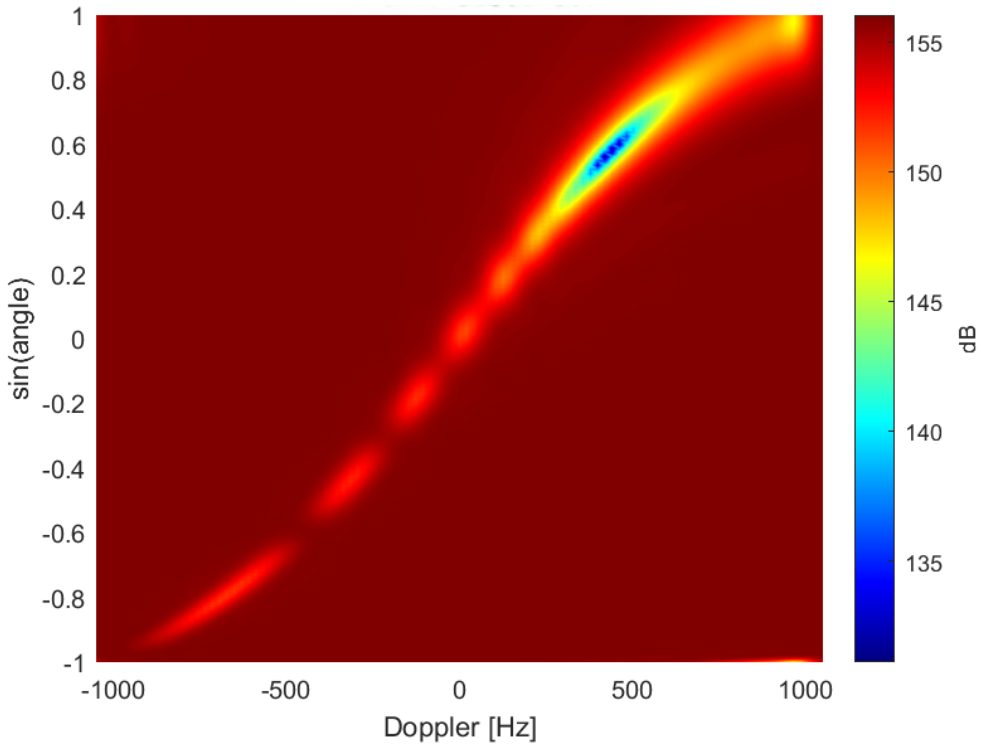

Modeling Inhomogeneous Clutter for Airborne Bistatic Radar Detection

Investigating inhomogenous clutter reflectivity patterns' impact on detector performance in airborne bistatic radar

Master's thesis in Information and Communication Technology

NEDA GHOLAMPOUR

DEPARTMENT OF Electrical Engineering
CHALMERS UNIVERSITY OF TECHNOLOGY
Gothenburg, Sweden 2024
www.chalmers.se

Master's thesis 2024

Modeling Inhomogeneous Clutter for Airborne Bistatic Radar Detection

Investigating inhomogenous clutter reflectivity patterns' impact on detector performance in airborne bistatic radar

NEDA GHOLAMPOUR

CHALMERS
UNIVERSITY OF TECHNOLOGY

Department of Electrical Engineering
Chalmers University of Technology
Gothenburg, Sweden 2024

Modeling Inhomogeneous Clutter for Airborne Bistatic Radar Detection
Investigating inhomogenous clutter reflectivity patterns' impact on detector performance in airborne bistatic radar
NEDA GHOLAMPOUR

Supervisor: Tomas McKelvey, Department of Electrical Engineering
Examiner: Tomas McKelvey, Department of Electrical Engineering

Master's Thesis 2024
Department of Electrical Engineering
Chalmers University of Technology
SE-412 96 Gothenburg
Telephone +46 31 772 1000

Typeset in LaTeX
Printed by Chalmers Reproservice
Gothenburg, Sweden 2024

Modeling Inhomogeneous Clutter for Airborne Bistatic Radar Detection
Investigating inhomogenous clutter reflectivity patterns' impact on detector performance in airborne bistatic radar

NEDA GHOLAMPOUR
Department of Electrical Engineering
Chalmers University of Technology

Abstract

Clutter suppression poses a significant challenge in space-time adaptive processing (STAP) for airborne radar systems due to the intricate nature of real-world scenarios. A key difficulty in clutter suppression arises from its heterogeneous nature, which is common in most cases. By assuming an identical reflectivity coefficient for received echoes from unwanted objects during the estimation of the covariance matrix, we introduce inaccuracies into our model.

Additionally, a bistatic radar configuration is more complex due to its distinct geometry compared to the simpler monostatic configuration (such as elliptical range) and separate velocities of the transmitter and receiver platforms, which causes more complexities to emerge. Despite these challenges, most existing studies primarily focus on addressing the range dependency of clutter spectrum, with insufficient emphasis on thoroughly exploring the inherent heterogeneity of clutter.

In this study, our main goal is to explore how different clutter reflectivity patterns affect different types of detectors' performance and by examining these variations we want to uncover how clutter impacts the accuracy and effectiveness of detection systems. Our aim is to identify scenarios where the performances of several types of detectors converge or meet.

Keywords: Airborne Bistatic Radar Systems, Space-Time Adaptive Processing.

Acknowledgements

First of all, I would like to extend my deepest gratitude to my supervisor Tomas McKelvey who provided me with the opportunity to work on this thesis and for his guidance and support. He was a true example of who a researcher should be and have been a source of inspiration for me throughout my journey. I am also grateful towards my family and friends for their unwavering support and encouragement and believing in me even when I did not.

Neda Gholampour, Gothenburg, June 03, 2024

Table of Contents

1

Introduction

1.1 Overview

Although it is hard to trace back the exact date that the modern radars originated from, there are some milestones indicating the development of today's radar systems. In 1888 Heinrich Hertz developed a basic principle for radars [1]; and in the early 1900s, Christian Hulsmeyer from Germany developed a device based on this principles to detect objects and it was tested on the detection of ships to prevent collision [2]. However for many years, there were not further investigation regarding this matter until mid 1930s. At that time there happened to be a world wide interest in radar development which is a response to the development of modern bomber aircraft and to prevent the damage it caused [1].

Apart from its application in military, radar serves a various of purposes in civilian life such as autonomous vehicles, weather forecasting, etc. The reason for its popularity and wide application is due to its advantages compared to its counterparts such as video cameras and lidar. Radars are advantageous due to their robustness to various weather condition, different lightning situations and the ability of detection in long ranges [3]. This is because they use electromagnetic waves and by observing the reflection of these waves, the location, speed and direction of movement of an object can be determined. In this thesis, the focus of research is on airborne radars which are mostly used in military applications.

Based on their application, radars are equipped with different hardware and software designs which would determine its performance. One choice in designing the hardware would be the number of array channels on the antenna. The directivity of a transmitter antenna and the spatial resolution of a receiver antenna are influenced by the number of array channels. In a multi-channel radar system, multiple antenna elements are used for transmission and reception. These elements can have various configuration such as uniform linear array (ULA) or uniform rectangular array (URA). These configuration allows beamforming and provides higher resolution.

Another hardware configuration consists of the choice of waveform. When implementing pulse waveform, the transmitter sends short bursts of electromagnetic energy and waits for the returning echos. The pulsed waveform are commonly used for long-range detection and accurate ranging measurements, however its effectiveness is limited at

very short ranges. The second choice of waveform is a continuous signal which requires less energy and is not limited at short distances. However, since there is a limit as how much the power can be transmitted, its detection range is limited. Frequency modulated continuous wave (FMCW) is another type of waveform which uses a continuous signal with varying frequency over time. This waveform is mostly used in autonomous vehicles applications and are not covered in this thesis. The waveform used in the configuration of this work is pulse waveforms.

Another configuration for radar hardware involves the placement of the transmitter and receiver. If the transmitter and receiver are co-located, it is a monostatic configuration. Conversely, when the transmitter and receiver are situated separately, this setup is referred to as a bistatic configuration. Although monostatic setup is widely used, there is a growing shift of interest towards bistatic configuration despite the complexities that this setup brings which are inherent to its geometry. This trend is caused by the unique advantages offered by the bistatic approach, such as its enhanced capability to detect low-observable targets and the fact that the receiver's location can remain hidden [4]. In this thesis, the primary focus will be on the bistatic configuration and its performance against various scenarios is investigated further.

Software of a radar system consists of signal processing algorithms. The signal received by the receiver consists of the data regarding one or multiple targets, however this signal is usually contaminated by various types of interference such as clutter, thermal noise and jamming. The purpose of such algorithms is to remove the interference and unwanted part from the received signal without cutting any energy from the useful part of signal.

The algorithm performance is affected by the quality of the received signal, the environmental scenario and the geometry. An algorithm can be called robust that is not dependant on a specific scenario and can be applied to all cases with an almost minimal change in performance provided that the signal energy is constant for all cases. That is why to test an algorithm, instead of using a deterministic case, statistically generated data are fed into the algorithm. This includes both for the signal corresponding to the target and the interference. In this thesis, specifically, the robustness is investigated against different ground clutter realizations. This line of inquiry is particularly important, as there has been limited investigation into the effects of heterogeneity of clutter in previous studies [5].

1.2 Literature Review

Limited research has been conducted on the heterogeneity of clutter. One of the studies that consider this phenomena is in [6]. It studies the effect of amplitude and spectral heterogeneity and the resulting mismatch in data on signal-to-noise-ratio and emphasizes the importance of considering these factors in space-time adaptive

processing for airborne radar systems. Also, it include moving scatterers to its model and presents the degradation in performance caused by it. In order to model the covariance matrix, accessing to extensive training data especially in heterogeneous backgrounds is needed which is challenging. A thinned space-time adaptive approach is proposed in [7] which requires less training data as it selects the ones that gives the highest performance. The performance of this method is evaluated in the presence of both homogeneous and heterogeneous clutter. One method that is commonly used to overcome heterogeneous clutter model is knowledge-aided space-time adaptive processor. This method consists of providing processor with additional information to aid with estimating an accurate model for covariance matrix. This method is further explained in [8], [9]. The focus of research in this thesis is to observe the effect of inhomogenous background on the performance of space-time adaptive processing algorithm in a bistatic configuration.

1.3 Thesis Outline

In chapter 2, fundamental principles of radar are explained. This chapter covers how radar systems work, including the physics behind radar detection and introduce the basics of signal processing and the space time adaptive processing (STAP) algorithm. Chapter 3 is dedicated to detection, specifically focusing on the presentation of various detectors and their distinctions. It describes the challenges introduced to the system by inhomogenous clutter model and details the development of the detection algorithm designed to overcome these challenges. Results are presented in chapter 4 and the last part contains conclusion of this thesis.

2

Radar Theory

To have a better understanding of the next topics, in this chapter, fundamentals of radar signal processing is discussed.

2.1 Radar Basics

In this part the basic theory of a radar for a monostatic configuration is explained however a more in depth relations for bistatic case can be found in [10].

Radar works by sending an electromagnetic wave and observing the received echo. Specifically, in case of pulsed Doppler radar, a series of pulses are sent as shown in Figure 10 and a portion of the transmitted energy is received by the receiver antenna. The received echo can give away many properties of the observed object such as its distance and radial velocity. The range can be determined by the time it takes the transmitted wave to be reflected by the target and received:

$$R = \frac{c\Delta t}{2} \tag{2.1}$$

In which c is the speed of light and Δt is the time it takes for the echo to be received and since it travels double the distance to the target it is divided by two. In order for the receiver to listen to the echos, the transmitter must be switched off. Hence, the pulses are send with an interval time called pulse repetition interval (PRI) which is indicated in the Figure 10 and the pulse repetition frequency (PRF) is given by:

$$PRF = \frac{1}{T_{PRI}} \tag{2.2}$$

It should be noted that in bistatic configuration, the challenge of simultaneously transmitting and receiving signals is mitigated by the spatial separation of the transmitter and receiver and other types of waveform can be used. However, despite this separation, the system still employs pulsed transmissions.

The Doppler effect allows for the determination of a moving object's velocity and whether or not it is moving towards the radar or away from it. Based on the object's

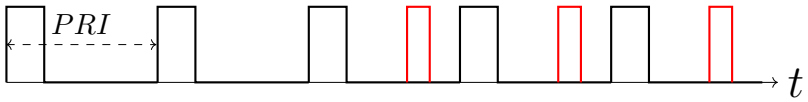

Figure 1: Transmitted and received pulses

direction, the signal may either be compressed or elongated. When the object is moving towards the radar, the signal becomes compressed; conversely, if it is moving away, the signal is stretched out which causes a shift in frequency. Using this shift the speed can be obtained from the expression below:

$$f_D = \frac{v}{\lambda} \tag{2.3}$$

In which, v is the speed of the moving object and $\lambda = c/f$ is the wavelength with c and f indicating the speed of light and carrier frequency of the radar system respectively.

The direction from the radar in which the target is located at can be obtained from the antenna array. However, the basics of an antenna array must be explained first. As discussed before, one possible configuration for antenna in radar is ULA which is also what is implemented in this thesis and consists of several antenna elements that are spaced equally along a straight line. This configuration has many benefits compared to a single element antenna such as directivity and high signal to noise ratio (SNR). The graphical representation of an ULA is shown in Figure 2 featuring N channels with distance d which can be less or equal to half of the wavelength. It is assumed that the scatterer is located at the far field region of the antenna so that the received echos are treated as planar wave. As it can be seen from the figure, the echo that reaches the nth element had covered an excess distance of $(n-1)d\cos\theta$. This extra distance causes a phase shift in the signal which is proportional to cosine of the incident angle θ which is how we can determine the direction of the target.

Lastly, assuming that propagation loss and system loss are zero, radar equation in the form of received power to the receiver for the monostatic configuration can be expressed as:

$$P_r = \frac{P_t G^2 \lambda^2 \sigma}{(4\pi^3) R^4} \tag{2.4}$$

This can be easily extended to the bistatic configuration:

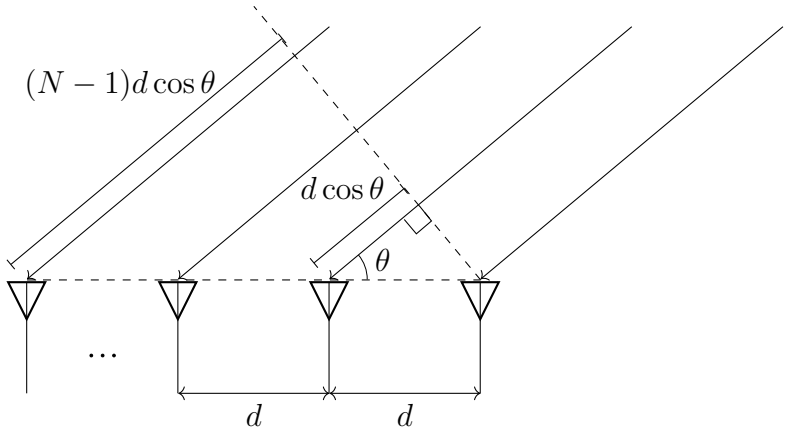

Figure 2: Uniform Linear Array

$$P_r = \frac{P_t G_t G_r \lambda^2 \sigma}{(4\pi^3) R_t^2 R_r^2} \tag{2.5}$$

Where P_r and P_t are received and transmitted power respectively and G_t stands for transmitter gain and G_r is for receiver gain. The distance to a point in space from transmitter is shown by R_t, and the range from the same point to receiver is denoted by R_r. σ indicates bistatic cross section.

2.2 Interference Types

As mentioned above, detection is done by processing the signal that reaches the receiver and this signal apart from a potential target, contains clutter interference, jamming interference and the thermal noise that comes from receiver. Since in this thesis the objective is to detect moving targets, clutter interference then refers to unwanted echos from stationary objects. In this type, these echos are caused by the electromagnetic waves transmitted by the transmitter in the system. Objects within the environment possess varying reflectivity coefficients, indicating that each reflects a distinct fraction of the radar signal that reaches them. This depends on the object properties such as its the material properties such as electrical conductivity and dielectric properties, shape, size and the surface roughness. It also depends on the grazing angle i.e. the angle between the beam and the surface.

However, in jamming interference, this disturbance is caused by an external source with the same working frequency band such as other systems transmitting in the vicinity of our radar system or is deliberately caused to block the receiver from detecting a target. In general jamming signal can have a high power due to its line-of-sight path to the receiver therefore it can be quite challenging to mitigate it.

2.3 Radar Signal Processing

In this part, we introduce the binary hypothesis testing used by the detector to determine target presence, along with the signal model and detection methods. We also present the STAP algorithm and matched filter implemented in this thesis.

2.3.1 Binary Hypothesis Testing

Consider $\boldsymbol{r}$ to be the measured signal in the receiver:

$$\boldsymbol{r} = \alpha \boldsymbol{s} + \boldsymbol{n} \tag{2.6}$$

In which $\alpha \boldsymbol{s}$ is the signal from a potential target and $\boldsymbol{n}$ is the contribution of the interference such as jamming, clutter and thermal noise and in case there is no target α is zero. It should be noted that since we can never predict their voltage, both α and $\boldsymbol{n}$ are random variables driven from a certain distribution which will be discussed later in signal model part. Therefor, it is detector's job to conclude whether there is a target, H_1, ($|\alpha| > 0$) or that there is no target, H_0, ($\alpha = 0$) which are the two outcomes. This is achieved by application of binary hypothesis testing. For the detector to decide between each of these hypothesises, a test statistic is formed and its value would be compared to a certain threshold. The test statistic, denoted as $\Lambda(\boldsymbol{r})$, is a function that helps in comparing the measured data against a threshold (γ).

To this end, it is also required to assign conditional densities $p_{\boldsymbol{r}|H}(\boldsymbol{r}|H_1)$ and $p_{\boldsymbol{r}|H}(\boldsymbol{r}|H_0)$ which indicates the distribution of measured data under these two hypothesis. Based on the test statistic decision, there can be four outcomes. The first two outcomes are for when the decision was correct meaning that if there was not target detector correctly chooses H_0 which is called correct rejection, and if there was a target, detector opted for H_1 and the target is detected. The third outcomes is called missed detection which means that there was a target but hypothesis H_0 was selected. Lastly is for when there is no target however H_1 is selected and is called false alarm. Out of the two error regions the former is particularly critical however the second error must be avoided as much as possible since the system has a specified tolerance for its occurrence.

This introduces the importance of selecting the optimal test statistic. One that has the highest probability of detection yet keeps the false alarm rate below a certain level. The probability of detection and false alarm can be calculated as show below:

$$P_D = P[H = H_1|H_1] = \int_{\boldsymbol{r}\in\Lambda(\boldsymbol{r})>\gamma} p_{\boldsymbol{r}|H}(\boldsymbol{r}|H_1)\, d\boldsymbol{r} \tag{2.7}$$

$$P_{FA} = P[H = H_1|H_0] = \int_{\boldsymbol{r}\in\Lambda(\boldsymbol{r})>\gamma} p_{\boldsymbol{r}|H}(\boldsymbol{r}|H_0)\, d\boldsymbol{r} \tag{2.8}$$

These integrals represent the areas under the probability density functions for the two hypotheses shown in Figure 3. The red region indicates P_D and the blue region represents P_{FA}. This figure marks the relation between P_D, P_{FA} and the threshold (γ). The smaller the choice of γ, P_D also increases, as good as it sound, it should be noted that P_{FA} also increases as well. This problem is cause due to the overlap of these two pdfs indicate uncertainty in the decision-making process.

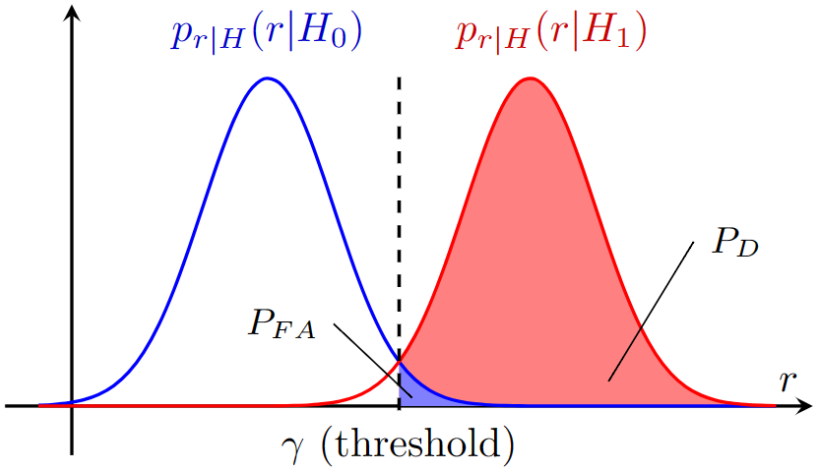

Figure 3: Pdfs of the hypothesis and the relation between P_{FA}, P_D and γ

To this end, the Neyman-Pearson criteria (NPC) is the most optimum framework despite this uncertainty and is commonly used [11]. This framework is specially useful when in reality we have no access to prior probabilities on H [11]. The likelihood ratio test (LRT) is an optimal method used to implement the NPC and is:

$$\Lambda(\boldsymbol{r}) = \frac{p_{\boldsymbol{r}|H}(\boldsymbol{r}|H_1)}{p_{\boldsymbol{r}|H}(\boldsymbol{r}|H_0)} \lessgtr \gamma \tag{2.9}$$

Therefore, LRT is the detector used in radar system which evaluates the ratio of probability density function (pdf) between these two hypothesis and compare the value with a certain threshold. If this ratio becomes higher than the threshold, then the alternative hypothesis, H_1 is declared as an answer, otherwise null hypothesis H_0 is approved.

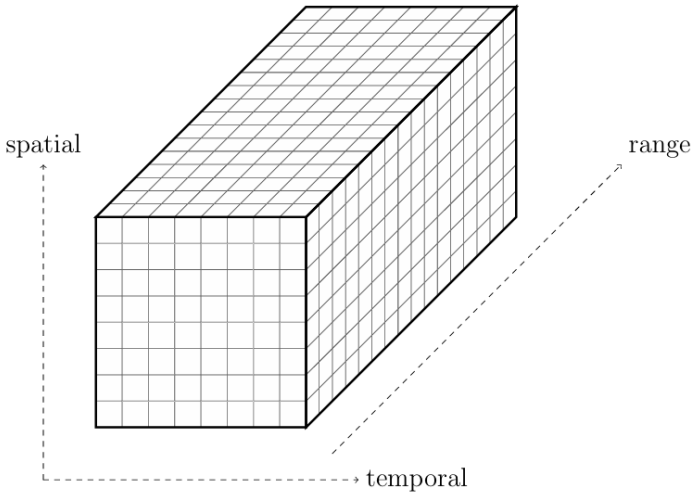

Figure 4: data cube $\mathbf{x} \in \mathcal{C}^{NMK}$

2.3.2 Signal Model and Detection

As mentioned before, in this thesis STAP will be used as a method of signal processing which is a two-dimensional filtering technique that combines spatial processing, using an array of antenna elements (N), with temporal processing which is related to the number of pulses (M) over which the signal is analyzed. These data are collected over several range bins (K), then the pulse compression scheme is applied in the fast time dimension, creating the observation $\mathbf{r} \in \mathcal{C}^{NMK}$. An illustration of this data cube is shown in Figure 4. The observation in every range bin is called a snapshot and is indicated as $\mathbf{r}_k \in \mathcal{C}^{NM\times 1} \forall k \in [0, K-1]$. Each of these snapshots consists of clutter signal $\mathbf{r}_{ck}$, jamming signal $\mathbf{r}_{jk}$, thermal noise $\mathbf{r}_{nk}$ and a potential target $\mathbf{r}_{tk} = \alpha_s \boldsymbol{s}_{st}$ with α_s being the magnitude of the target and $\boldsymbol{s}_{st}$ the space-time steering vector of target. This vector points toward the angle and Doppler frequency from which the target signal originates.

In this thesis it is assumed that clutter, jamming and thermal noise signals are modeled from complex Gaussian distribution with mean value of zero and their respective covariance matrix. Assume that receiver is performing detection on the received signal $\boldsymbol{r}_k$ from a certain range bin which can be called cell under test (CUT) and it must select between the two hypothesis. The received signal under these two hypothesis is shown as:

$$\mathbf{r}_k|H_0 = \mathbf{r}_{ck} + \mathbf{r}_{jk} + \mathbf{r}_{nk} \quad \text{with pdf} \quad p_{\boldsymbol{r}_k|H}(\boldsymbol{r}|H_0) = \mathcal{CN}(0, \boldsymbol{R}_k) \tag{2.10}$$

$$\mathbf{r}_k|H_1 = \mathbf{r}_{tk} + \mathbf{r}_{ck} + \mathbf{r}_{jk} + \mathbf{r}_{nk} \quad \text{with pdf} \quad p_{\boldsymbol{r}_k|H}(\boldsymbol{r}|H_1) = \mathcal{CN}(\boldsymbol{r}_{tk}, \boldsymbol{R}_k) \tag{2.11}$$

In which, $\boldsymbol{R}_k$ is the total covariance matrix. Since we assumed that these interference are independent of each other then R_k is obtained from the sum of each of the covariance matrices: $\boldsymbol{R}_k = \boldsymbol{R}_{ck} + \boldsymbol{R}_{jk} + \boldsymbol{R}_{nk}$.

To perform this decision making, the signal is multiplied by a weighting function, $\boldsymbol{w}$ which yields the weighted sum of all elements of the signal. This operation is called applying monotonic operation so that the complexities of LRT detector which was presented above is reduced [11]. The resulting LRT detector would then be: $y_k = |\boldsymbol{w}_k^H \boldsymbol{r}_k| \lessgtr \gamma$ with y_k being a scalar. In this expression H indicates Hermitian transpose and $|.|$ denotes absolute value.

Since $\boldsymbol{w}$ role is to remove unwanted parts of a signal while preserving the ideal part of it, finding the best weight vector is of upmost importance therefore there should be a performance metric defined to evaluate the selected $\boldsymbol{w}$. Signal-to-Interference-plus-Noise Ratio (SINR) is one of such metrics which measures the power ratio between the desired signal and the sum of the interference power from other sources such as clutter and the power of the background noise. It quantifies how well a receiver can distinguish the desired signal from noise and clutter. Given that SINR has a direct relationship with the performance of a detector, with a higher SINR indicative of better performance, the objective is to achieve a higher SINR.

Depending on the choice of $\boldsymbol{w}_k$, different detectors are obtained. The weight that yields maximum SINR is obtained from: $\boldsymbol{w}_k = \mu \boldsymbol{R}_k^{-1} \boldsymbol{s}_{st}$ [11]. μ is an arbitrary constant that does not affect SINR and as mentioned before, $\boldsymbol{s}_{st}$ is the target steering vector and is a Kronecker product between space vector and time vector $\boldsymbol{s}_{st} = \boldsymbol{s}_t(f_d) \otimes \boldsymbol{s}_s(f_s)$. Although as mentioned μ can be selected arbitrary, certain choices of this value can bring some conveniences. One common detector is matched filter with: $\mu = 1/\sqrt{\boldsymbol{s}_{st}^H \boldsymbol{R}_k^{-1} \boldsymbol{s}_{st}}$ which would yield the optimal detector with the expression shown below:

$$y_k^2 = |\boldsymbol{w}_k^H \boldsymbol{r}_k|^2 = \frac{|\boldsymbol{s}_{st}^H \boldsymbol{R}_k^{-1} \boldsymbol{r}_k|^2}{\boldsymbol{s}_{st}^H \boldsymbol{R}_k^{-1} \boldsymbol{s}_{st}} \lessgtr \gamma \tag{2.12}$$

In this detector, it is assumed that we have full access to the true covariance matrix. However, since in real case scenarios, this assumption is not correct, a general case of weight vector can be presented in the form of $\boldsymbol{w}_k = \hat{\boldsymbol{R}}_k^{-1} \boldsymbol{s}_{st} / \sqrt{\boldsymbol{s}_{st}^H \hat{\boldsymbol{R}}_k^{-1} \boldsymbol{s}_{st}}$, which matches an estimation of the covariance matrix to the true one. This weight vector would give us the general form of a detector:

$$y_k^2 = |\boldsymbol{w}_k^H \boldsymbol{r}_k|^2 = \frac{|\boldsymbol{s}_{st}^H \hat{\boldsymbol{R}}_k^{-1} \boldsymbol{r}_{st}|^2}{\boldsymbol{s}_{st}^H \hat{\boldsymbol{R}}_k^{-1} \boldsymbol{s}_{st}} \lessgtr \gamma \tag{2.13}$$

By replacing $\hat{\boldsymbol{R}}_k$ with $\boldsymbol{R}_k$, optimal detector, (2.12), is obtained.

2.3.3 Space-Time Adaptive Processing

In the previous part the optimal detector which gives the highest SINR possible was introduced. However, in real scenarios, $\boldsymbol{R}_k$ is unknown. This is where STAP algorithm becomes important as it is a data driven algorithm that tries to find the most optimum weighting from the data to achieve the closest results to optimal SINR.

This algorithm uses secondary data, the observations that are received from other range bins outside CUT to estimate the covariance matrix. It is assumed that there is no target outside of CUT so these returns are only from clutter and from thermal noise and the signals $\boldsymbol{r}_k \forall k \in [1, K]$ fall under the null hypothesis. Also, in most cases the thermal noise power in the receiver, σ_n^2, is assumed to be known and its respective covariance matrix can be modeled. As such, the covariance matrix for null hypothesis which models the clutter and thermal noise is driven from the expression below. However, this expression only holds for monostatic radar, as covariance matrix for a bistatic setup is range dependant.

$$\hat{\boldsymbol{R}}_0 = \frac{1}{K-1} \sum_{k=1}^{K-1} \boldsymbol{r}_k \boldsymbol{r}_k^H \tag{2.14}$$

The generalized SINR form for when there is a possibility of mismatch between estimated covariance matrix and the true one would be:

$$\text{SINR} = \frac{|\boldsymbol{s}_{st}^H \hat{\boldsymbol{R}}_k^{-1} \boldsymbol{s}_{st}|^2}{\boldsymbol{s}_{st}^H \hat{\boldsymbol{R}}_k^{-1} \boldsymbol{R}_k \hat{\boldsymbol{R}}_k^{-1} \boldsymbol{s}_{st}} \leq \boldsymbol{s}_{st}^H \boldsymbol{R}_k^{-1} \boldsymbol{s}_{st} \tag{2.15}$$

It can be simply proven that in case the estimated covariance matrix matches the true one, the SINR would then convert to optimal SINR which is equal to $\boldsymbol{s}_{st}^H \boldsymbol{R}_k^{-1} \boldsymbol{s}_{st}$ and in turn, the differences between these two covariance matrices i.e. $||\boldsymbol{R}_k - \hat{\boldsymbol{R}}_k|| > 0$ can result in SINR loss.

2.4 Kullback-Leibler Divergence

A method to compare different detectors (besides comparing the SINR) is by measuring the distance between their covariance matrices. Kullback-Leibler Divergence (KLD) is a measure of how two probability distribution functions are different from one another and is denoted by $D_{KL}(p||q)$ with $p(x)$ being the true distribution. Both these PDFs are defined on the same sample space $\mathcal{X}$ and the KLD between them is defined by

[12],[13]:

$$D_{KL}(p||q) = \int_{x\in\mathcal{X}} p(x)\log(\frac{p(x)}{q(x)})dx \tag{2.16}$$

If both p and q are normally distributed with the same mean value, then KLD is only affected by their covariance matrices and equation (2.16) can be rewritten as:

$$D_{KL}(p||q) = \log(\det(\boldsymbol{R}_q)) + \mathrm{tr}(\boldsymbol{R}_p\boldsymbol{R}_q^{-1}) - \log(\det(\boldsymbol{R}_p)) - K \tag{2.17}$$

In which $\boldsymbol{R}_p$ and $\boldsymbol{R}_q$ are the covariance matrices of p and q respectively and their common subspace is $\mathcal{C}^K$. So if $p = q$ then this equation would be equal to zero. It should be noted that the expression (2.16) is asymmetric, meaning that $D_{KL}(p||q)$ is not necessarily equal to $D_{KL}(q||p)$. Using KLD, it can be analyzed how different detectors perform for a certain scenario. The matrix $\boldsymbol{R}_p$ is replaced by the true covariance matrix, which corresponds to the optimal detector, and $\boldsymbol{R}_q$ represents either $\boldsymbol{R}_{sub}$ for subspace or the estimated covariance matrix for a suboptimal detector.

It should be noted that SINR is upper bounded by a detector that uses the correct covariance matrix in the weight vector. This highlights the connection with KLD, as comparing each of the covariance matrices to the optimal one (true covariance matrix) allows us to see how much distance they have from the optimal covariance matrix and how much their performance degrades compared to the highest SINR. However, while KLD provides a measure of distance, it does not always guarantee that a suboptimal detector with a smaller KLD will always perform better than another suboptimal detector.

3

Methods

In this section, the detailed algorithm for modelling the scenario, clutter and its covariance matrix is explained. Afterwards, an overview of the proposed detector would be provided.

3.1 Radar Geometry

A bistatic geometry is depicted in Figure 5, and in it Tx and Rx denote the transmitter and receiver respectively. A target is marked as Trg which is located above the ground and the clutter patch is indicated by P_s and its location is determined by four parameters $(\theta_T, \varphi_T, \theta_R, \varphi_R)$ with θ_T and φ_T being elevation and azimuth angles between the clutter and the transmitter while θ_R and φ_R indicating elevation and azimuth angles between the clutter and the receiver. One additional point that should be mentioned but is not depicted in the figure, is that the angle of heading for the transmitter, in both elevation and azimuth is defined as $(\theta_{vt}, \varphi_{vt})$ and the angle of heading for the receiver is $(\theta_{vr}, \varphi_{vr})$.

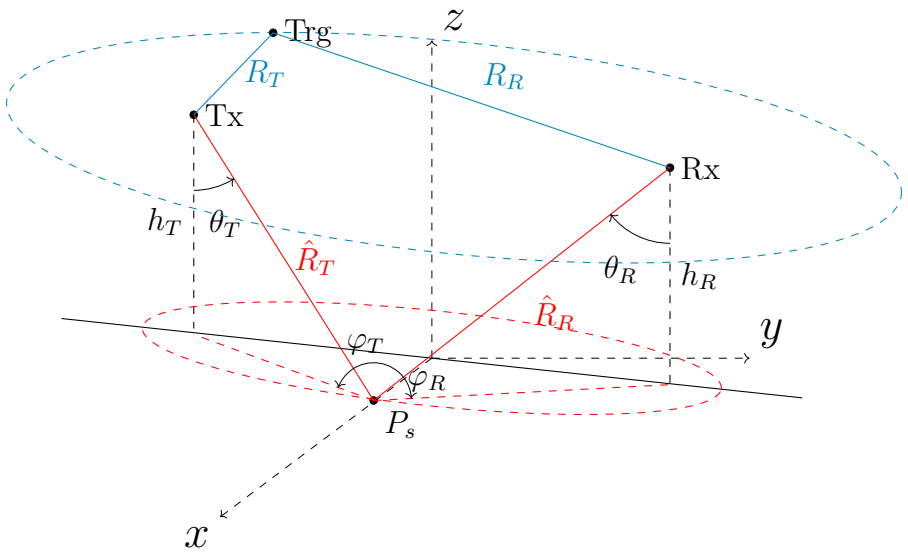

Figure 5: Bistatic radar geometry

In a bistatic geometry and for one range bin, the two platforms create an ellipsoid with the two focal points being Tx and Rx. This means that for any point on the ellipsoid

the sum of the distances to the Tx and Rx is constant, also called the bistatic range. This ellipsoid in 3D space would have the equation of:

$$(\frac{x-x_i}{a'})^2 + (\frac{y-y_i}{b'})^2 + (\frac{z-z_i}{c'})^2 = 1 \tag{3.1}$$

The intersection of this ellipsoid with ground surface which is assumed to be flat is an ellipse which contains the clutter patches that return a portion of transmitted signal as a clutter interference. The ground ellipse has a function defining it. The general parametric equation of an ellipse in 3D space is given by the expression:

$$\boldsymbol{f}_{ellipse} = \boldsymbol{f}_0 + \boldsymbol{f}_1 \cos t + \boldsymbol{f}_2 \sin t \quad \text{for} \quad 0 < t < 2\pi \tag{3.2}$$

In which $\boldsymbol{f}_0$ is the center and $\boldsymbol{f}_1$ and $\boldsymbol{f}_2$ are the vectors from the center to a point on the ellipse with maximum and minimum curvature respectively and are perpendicular to each other. The goal is to determine the parameters defining clutter ellipse which involves coordinate transformation[14]. To this end, firstly, both platforms must be projected on the ground and their distance on that plane is called d. It should be noted that the minimum bistatic distance that make an intersection with the ground would be: $D_{min} = \sqrt{(h_T + h_R)^2 + d^2}$ with h_T and h_R indicating the altitude of T_x and R_x respectively. If the bistatic distance, D_b is equal to D_{min} this intersection would be a point.

Afterwards, the coordinate origin must be shifted so that the origin point is located at midpoint between the two platforms. With this shift, the ground plane would be placed below the new coordinate system. next, the coordinate system is rotated with rotation matrix $\boldsymbol{R}_{rot}$ so that the line connecting T_x to R_x is aligned with the x-axis. This would turn the equation (3.1) to this expression:

$$(\frac{x}{a})^2 + (\frac{y}{b})^2 + (\frac{z}{c})^2 = 1 \tag{3.3}$$

If we define the distance between the two platforms as r, then $a = D_b/2$ and $b = c = \sqrt{a^2 - (0.5r)^2}$. Next, the coordinate system must be scaled so that the ellipsoid would become a sphere with a unit radius and the newly transformed ground plane intersecting this sphere creates a circle with the equation: $\boldsymbol{r}(t) = \boldsymbol{r}_0 + \boldsymbol{r}_1 \cos t + \boldsymbol{r}_2 \sin t$ with $|\boldsymbol{r}_1| = |\boldsymbol{r}_2|$.

The ground plane which has gone through translation, rotation, and scaling will be described by two vectors; a normal vector $\boldsymbol{n}'$ and distance vector $\boldsymbol{d}'$. $\boldsymbol{n}'$ can be calculated

by rotating the round plane so that it is parallel to xy-plane and the clutter circle will have the expression: $\boldsymbol{z}(t) = \boldsymbol{z}_0 + \boldsymbol{z}_1 \cos t + \boldsymbol{z}_2 \sin t$ with $|\boldsymbol{z}_0| = |\boldsymbol{d}'|$ and $|\boldsymbol{z}_1| = |\boldsymbol{z}_2| = \sqrt{1 - |\boldsymbol{d}'|^2}$. Once $\boldsymbol{z}(t)$ is obtained, the reverse transformations are applied to retrieve $\boldsymbol{r}(t)$ from $\boldsymbol{z}(t)$ thereby achieving $\boldsymbol{f}_{ellipse}$ as described in equation (3.2).

3.2 Clutter Modelling

In this part the variables defining clutter are explained individually. Each clutter patch has a characteristic that is defined by its space steering vector $\boldsymbol{s}_s$, time steering vector $\boldsymbol{s}_t$, its distance to the receiver and the transmitter R_R, R_T, its reflectivity coefficient σ^0 and the bistatic distance $D_b = R_T + R_R$ and it generates the signal:

$$\boldsymbol{r}_{ck_i} = \alpha \sqrt{\sigma^0 \frac{G_T(\theta_0, \theta_c) G_R}{R_T^2 R_R^2} dA} \boldsymbol{s}_{st} \tag{3.4}$$

In which G_T and G_R are the transmitter and receiver gains respectively and dA represents the area of each cell around the bistatic ellipse. The non-negative real value σ^0 is the reflectivity coefficient. Later on we will model the clutter reflectivity $\sigma^0(x, y)$ as a field i.e. a function that depends on the absolute position of the clutter patch. Steering vector is denoted by $\boldsymbol{s}_{st}$. For each point in the ellipse the steering vector must be calculated and as mentioned before, it is the result of the Kronecker production of time and space steering vectors. To model the random phase and amplitude of the clutter return, α is a zero mean complex circularly symmetric random variable with unit variance. Hence, r_{ck_i} is a zero mean random vector. Further we assume that the clutter return for different patches are uncorrelated.

3.2.1 Space Steering Vector

When a signal reaches the ULA antenna it will face phase shift at each element that can be modeled by space steering vector which has the form:

$$\boldsymbol{s}_s(f_s) = [1, \exp(j2\pi f_s), ..., \exp(j2\pi(N-1)f_s)]^T \tag{3.5}$$

With N being the number of receiver antenna elements and f_s defining the normalized spatial frequency. In this thesis both antennas implemented in both platforms are ULA, oriented parallel to the longitude of the respective platforms so f_s would have the format: $f_s = \frac{d}{\lambda} \mathbf{d}_{Rx}^T \mathbf{d}_{RxP_s}$. d denotes the spacing between antenna elements, while $\mathbf{d}_{RxP_s}$ and $\mathbf{d}_{Rx}$ are unit norm vectors. With the former being the vector pointing from the receiver to the clutter patch, and the latter representing the heading vector of the receiver platform.

3.2.2 Time Steering Vector

A time steering vector models the phase shift between received pulses and depend on PRI and normalized Doppler frequency f_d and has the format of:

$$\boldsymbol{s}_t(f_d) = [1, \exp(j2\pi f_d T_{\text{PRI}}), ..., \exp(j2\pi(M-1)f_d T_{\text{PRI}})]^T \tag{3.6}$$

With M being the number of pulses. The bistatic Doppler frequency for each clutter patch depends on heading direction of both Tx and Rx represented with the unit norm vectors $\mathbf{d}_{Tx}$ and $\mathbf{d}_{Rx}$ as well as their respective velocities, v_t and v_r:

$$f_d = \frac{v_t}{\lambda}\mathbf{d}_{Tx}^T\mathbf{d}_{TxP_s} + \frac{v_r}{\lambda}\mathbf{d}_{Rx}^T\mathbf{d}_{RxP_s} \tag{3.7}$$

Here, $\mathbf{d}_{TxP_s}$ and $\mathbf{d}_{RxP_s}$ denote the unit norm vectors pointing from the transmitter to the clutter patch and from the receiver to the clutter patch, respectively.

3.2.3 Antenna gain

In this work it is assumed that both receiver and the transmitter utilize ULA antennas. The receiver antenna elements have zero phase shift between them, resulting in isotropic antenna gain. In contrast, the transmitter antenna achieves beam steering to a certain cone angle θ_0 by applying element-specific phase shifts. In both Tx and Rx, antenna's elements are spaced at certain intervals denoted by d and the ULA direction is aligned with the heading direction of the platform. Assuming that the transmitter antenna array consists of N_t elements, the amplitude gain of in the direction of θ_c is given by:

$$g_T(\theta_0, \theta_c) = \sum_{n=0}^{N_t-1} \exp(-j2\pi jn\frac{d}{\lambda}(\cos\theta_0 - \cos\theta_c)) \tag{3.8}$$

The power gain of this platform is the given by:

$$G_T(\theta_0, \theta_c) = |g_T(\theta_0, \theta_c)|^2 = \frac{\sin^2[N_T\pi(d/\lambda)(\cos\theta_0 - \cos\theta_c)]}{\sin^2[\pi(d/\lambda)(\cos\theta_0 - \cos\theta_c)]} \tag{3.9}$$

And if we want to calculate the gain at a certain clutter patch then: $\cos\theta_c = \cos(\varphi_{vt} - \varphi_T)$. In this work, the target is positioned at the broadside of the transmitter antenna therefore the main beam, θ_0, points toward the target.

3.3 Interference Covariance Matrix

The covariance matrix for a certain range bin k is given by:

$$\mathbf{R}_k = \mathbf{R}_{C_k} + \mathbf{R}_n = \int_\Omega \sigma^0 \frac{G_T(\theta_0, \theta_c) G_R}{R_T^2 R_R^2} \mathbf{s}_{st} \mathbf{s}_{st}^H dA_\Omega + \sigma_n^2 \mathbf{I} \tag{3.10}$$

As an analytical solution to the integral is not available, this expression can be approximated as the finite sum for L segments along the ellipse, each representing the angle $t = 2l\pi/L$ and the area of $dA = \frac{2\pi}{L}||\boldsymbol{f}_2 \cos t - \boldsymbol{f}_1 \sin t||$. The estimated expression then is:

$$\mathbf{R}_k = \frac{2\pi}{L} \sum_{l=0}^{L-1} \sigma^0 \frac{G_T(\theta_0, \theta_c) G_R}{R_T^2 R_R^2} \mathbf{s}_{st} \mathbf{s}_{st}^H ||\boldsymbol{f}_2 \cos t - \boldsymbol{f}_1 \sin t|| + \sigma_n^2 \mathbf{I} \tag{3.11}$$

3.4 Background Modelling

The type of background clutter modeling has a significant effect on the designed radar detection performance. Therefore, it matters that the choice of background modelling to be as close to real world scenarios as possible. In [15] it has been concluded that Weibull distribution is fitted the best to the actual data. In this simulation, the model used for background realization is defined as Weibull distribution for the amplitude of reflectivity coefficient and the phase is assumed to be uniformly distributed in the interval of $[0, 2\pi]$. In case that its shape parameter is equal to 2, the mean value of Weibull distributed clutter coefficient across all range bins is equal to Rayleigh. Hence, in order to compute the clutter covariance matrix, we create a ground plane containing reflectivity coefficients as a function that depends on the position. These coefficients are firstly derived from complex Gaussian distributed data, with a mean of 0 and a standard deviation of 1.

Following that, the next procedure involves transforming these uncorrelated data into data with correlated power characteristics by employing a 2-dimensional filter with a specified correlation length along both x and y axes. Applying the filter defined in (3.12) will give us an auto-covariance matrix with a certain correlation length along both axes.

$$h(x, y) = \exp\left(\frac{-|x|^2}{\varrho_x^2} + \frac{-|y|^2}{\varrho_y^2}\right) \tag{3.12}$$

In this expression ϱ_x and ϱ_y are the correlation lengths in both x and y axes respectively

and as shown before, reflectivity coefficient can be defined as σ^0. Before applying this matrix to the uncorrelated data, to generalize the background more, $h(x, y)$ can be rotated to a certain angle which can give a diagonally correlated background. The obtained window is then applied to the uncorrelated data, $U(x, y) \in \mathcal{CN}(0, 1)$, with a 2-Dimensional convolution:

$$\sigma(x, y) = h(x, y) * U(x, y) = \sum_i \sum_j h(i, j)U(x - i, y - j) \tag{3.13}$$

With the resulting $\sigma(x, y)$ having a zero-mean complex Gaussian distribution. At the end, the magnitude of these values is taken to achieve the Rayleigh-distributed data i.e. $\sigma^0(x, y) = |\sigma(x, y)|$ which gives the background reflectivity. This σ^0 is then inserted in the equation (3.10). Based on the initial draw of $U(x, y) \in \mathcal{CN}(0, 1)$ a new background realization would be generated and one realization can be seen in Figure 6.

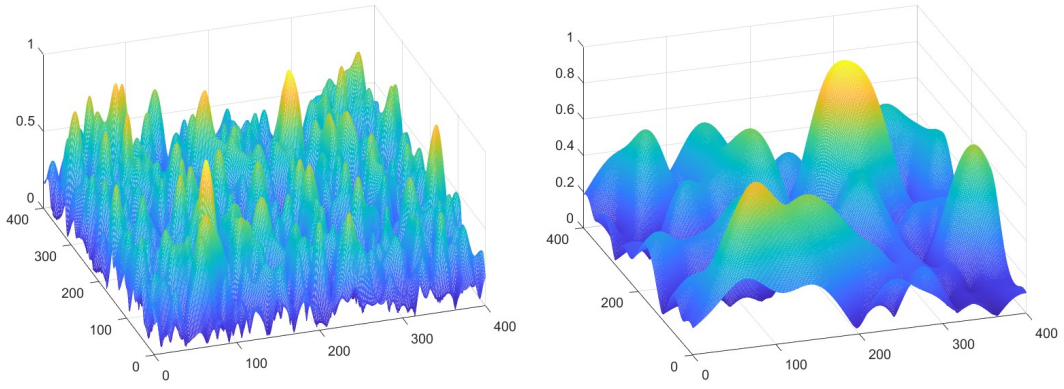

(a) correlation length = 10 Km (b) correlation length = 40 Km

Figure 6: Background realization, $\sigma^0(x, y)$

This type of defining background realization gives a relatively smooth surface with around 30 dB difference between the most and the least coefficients. To achieve even more difference between maximum and minimum reflectivity, a non-linear transformation can be performed on the final matrix containing the coefficients. One such transformation can be defined as:

$$\sigma_s^0(x, y) = 10^{(-10\sigma^0(x,y))} \tag{3.14}$$

It can be interpreted as amplifying the amplitudes in dB format and bringing them back to normal numbers which gives this new surface, $\sigma_s^0(x, y)$, a more spiky texture. One example of this field is shown in Figure 7.

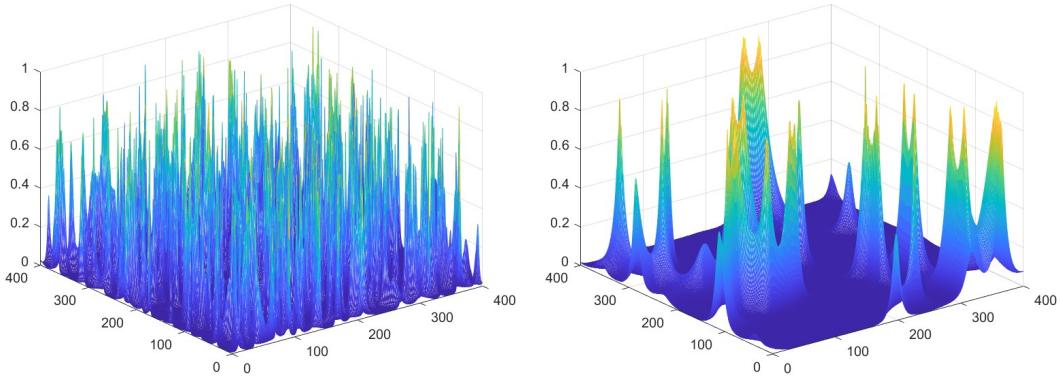

(a) correlation length = 10 Km (b) correlation length = 40 Km

Figure 7: Background realization, $\sigma_s^0(x, y)$

3.5 Types of detectors

In this thesis, different detector types are implemented and then their performance in terms of SINR is compared to that of optimal detector which gives the highest performance among all of them and it is not possible to achieve a SINR higher than that. As mentioned in section 2.3.2, several detectors are defined based on the choice of the weight vector w_k. In this section, the characteristics and implementation details of these detectors are discussed.

3.5.1 Optimal Detector

In the previous part it was shown that SINR can be achieved by equation (2.15) and that the difference between the true covariance matrix and the estimated one cause loss in performance. In this type of detector, it is assumed that the true covariance matrix for the inhomogenous background can be accessed by the receiver. Therefore, the SINR expression would turn out to be:

$$\text{SINR}_{opt} = \boldsymbol{s}_{st}^H \boldsymbol{R}_k^{-1} \boldsymbol{s}_{st} \tag{3.15}$$

This detector acts as an upper bound for all detectors.

3.5.2 Suboptimal Detector

To this detector, the true covariance matrix is unknown so it opts for an estimation of it. Since there is no knowledge about the background, it is assumed that the clutter reflectivity is homogeneous i.e. $\sigma^0(x, y) = \sigma^0$. It then matters to select a σ_0 that give the lowest SINR loss. To this end, one approach is to maximize the likelihood function for the secondary data. By maximizing the likelihood function, we aim to find the

value of σ_0 that results in the best fit between the estimated covariance matrix and the secondary data. This ensures that the selected σ_0 minimizes the loss in SINR and that the returned clutter power would be close to the real case.

3.5.3 Subspace

The subspace detector is a method used in radar signal processing to selectively remove specific directions of interference from covariance matrix, while retaining those where thermal noise plays a more significant role compared to clutter.

In a covariance matrix, a high eigenvalue associated with a particular direction means significant disturbance in that direction. Such disturbance can lead to substantial errors. Therefore, one approach is to address this issue is by completely removing the affected direction. On the other hand when the cancelled direction actually has a lower weight in disturbance but in the estimated covariance matrix there is a higher weight assigned to it, then aside from the interference, a part of the received signal containing information regarding target would be removed as well which will lead to worse result in SINR evaluation in suboptimal case.

To overcome this loss of important information, one way is to only remove the direction with high interference involved and not to cancel the directions that the thermal noise plays a more significant role compared to clutter since it is possible that in the estimated covariance matrix the weigh assigned to these directions are higher that the actual scenario. This method is called subspace detector which only removes certain directions of interference.

In this method, contrary to suboptimal method which uses the estimated covariance matrix, $\hat{\mathbf{R}}_k$, the estimated covariance matrix is truncated so that only the directions with highest eigenvalues are attenuated. The SINR value for this method is calculated by equation (2.15) and substituting the estimated covariance matrix by:

$$\mathbf{R}_{sub} = \sum_{1}^{r} (\lambda_i + \sigma_n^2)\mathbf{c}_i\mathbf{c}_i^H + \sum_{r+1}^{N} \sigma_n^2 \mathbf{c}_i\mathbf{c}_i^H \tag{3.16}$$

$\mathbf{c}_i$ and λ_i are the ith eigenvector and eigenvalue of $\hat{\mathbf{R}}_k$. These eigenvectors come from the estimated covariance matrix for suboptimal detector which has assumed a homogeneous background reflectivity. There are several types of selection for λ_i. One is to assume $\lambda_i \to \infty \forall i \in [0, r]$ which is called subspace 1 method and as for the second method, λ_i would be fixed to a certain value for all r ranks. Lastly in the third method, λ_i would be the same as the first r rank eigenvalues of the suboptimal detector.

Apart from the best selection for rank r, the second method needs another extra estimation for selecting the right fixed value, λ_D, to achieve the maximum performance. As mentioned previously, to have fair comparison between these methods, the returned clutter power for the real scenario and for the estimated covariance matrix that assumes a homogeneous background should be equal. This scaling value as well as r and λ_D are defined as explained below from KLD distance.

For suboptimal detector the scaling of clutter power is done so that the KLD distance become minimum. Likewise, for subspace 2 detector, a 2-dimensional optimization is done to achieve the lowest KLD by the best choice of rank and λ_D. Since it is not possible to calculate the rank for subspace 1 via this method, the same r used for the second subspace is also implemented here.

3.6 Parameter Estimation

Clutter covariance matrix depend on many parameters such as transmitter and receiver position and velocity as well as clutter reflectivity. Up until now, it was assumed that receiver knows all these information which is not true in real case scenario unless there is a direct line of communication between transmitter and receiver. However this will increase the risk of transmitter being exposed. Therefore, parameters relating to transmitter that are unknown to the receiver must be estimated using the secondary data so that it can estimate the covariance matrix based on them. The clutter covariance matrix model obtained from a parameter vector $\boldsymbol{\xi} = [x_T, y_T, z_T, |v_T|, \theta_{vt}, \varphi_{vt}, \theta_0]$ is given by:

$$\mathbf{R}_{C_k}(\boldsymbol{\xi}) = \int_{\Omega} \sigma^0 \frac{G_T(\theta_0, \theta_c) G_R}{R_T^2 R_R^2} \mathbf{s}_{st} \mathbf{s}_{st}^H dA_{\Omega} \tag{3.17}$$

The method implemented in [16] is used to estimate the parameter vector which uses maximum likelihood estimation (MLE). The problem is formulated as shown below:

$$\max_{\boldsymbol{\xi}} \ln L(\boldsymbol{\xi}|\mathbf{r}) \tag{3.18}$$

With L defining the null hypothesis distribution's likelihood function which uses the secondary data belonging to the range bins other that the CUT: $\boldsymbol{r}_k \forall k \in [1, K]$. Assuming that there is no target in those range bins, $\boldsymbol{r}_k$ belong to null hypothesis and have a normal distribution. So the likelihood function from (3.18) is expressed as:

$$\ln L(\boldsymbol{\xi}|\mathbf{r}) = \sum_{k=1}^{K} -(\ln\left(\det(\boldsymbol{R}_k(\xi))\right) + \boldsymbol{r}_k^H \boldsymbol{R}_k^{-1}(\boldsymbol{\xi})\boldsymbol{r}_k) - NM\pi \tag{3.19}$$

With the estimated parameter vector $\hat{\boldsymbol{\xi}}$ being obtained from:

$$\hat{\boldsymbol{\xi}} = \arg\min_{\boldsymbol{\xi}} \ln L(\boldsymbol{\xi}|\mathbf{r}) = \sum_{k=1}^{K} (\ln\left(\det(\boldsymbol{R}_k(\boldsymbol{\xi}))\right) + \boldsymbol{r}_k^H \boldsymbol{R}_k^{-1}(\boldsymbol{\xi})\boldsymbol{r}_k) \tag{3.20}$$

To this end the optimization algorithm is fed with the initial guess of variables, $\boldsymbol{\xi}_0$. The resulting $\hat{\boldsymbol{\xi}}$ depends on the choice of $\boldsymbol{\xi}_0$. If initial variables are chosen close to the real values, the algorithm might give the global minimum. However, if these values are selected far from the reality, algorithm might converge to a local optimum which gives the wrong covariance matrix and causes degraded performance. The number of available secondary data will also influence the result. With more and more data, the argument of the global minimum will converge to the true parameter values if the data is indeed generated according to the model assumptions. In the case when we use secondary data from the inhomogeneous clutter scenario and use the homogeneous clutter model, the arguments of the global optimum might differ from the true parameter values corresponding to the Tx platform position, velocity, etc.

4

Results

In this section, the method in previous section would be simulated and the results for various scenarios are presented. Table 1 and 2 contain system properties of both the transmitter and receiver for different experiments which is used to derive the results below. Both background types explained in the previous section would be used with the smooth changing background being referred to as type I and the other as type II. In some cases, several different realizations of these backgrounds with a certain correlation length are analyzed.

	Scenario			
Radar Parameter	**1**	**2**	**3**	**4**
Antenna peak gain in Tx	12 dB	12 dB	12 dB	12 dB
Number of Tx channels	1	16	16	16
Number of Rx channels	20	20	20	20
Number of pulses	20	20	20	20
Antenna gain in receiver	0 dB	0 dB	0 dB	0 dB
Antenna element spacing	0.025 m	0.025 m	0.025 m	0.025 m
Pulse repetition frequency	2100 Hz	1400 Hz	2100 Hz	1400 Hz
Wavelength	0.05 m	0.05 m	0.05 m	0.05 m
Thermal noise power in Rx	-130 dB	-130 dB	-130 dB	-130 dB
Transmitter's speed ($\|v_T\|$)	25 m/s	25 m/s	25 m/s	25 m/s
Receiver's speed ($\|v_R\|$)	25 m/s	25 m/s	25 m/s	25 m/s
Heading angle difference	0°	0°	0°	45°
Distance between platforms	0 Km	40 Km	40 Km	40 Km

Table 1: Radar parameters for scenarios 1 to 4

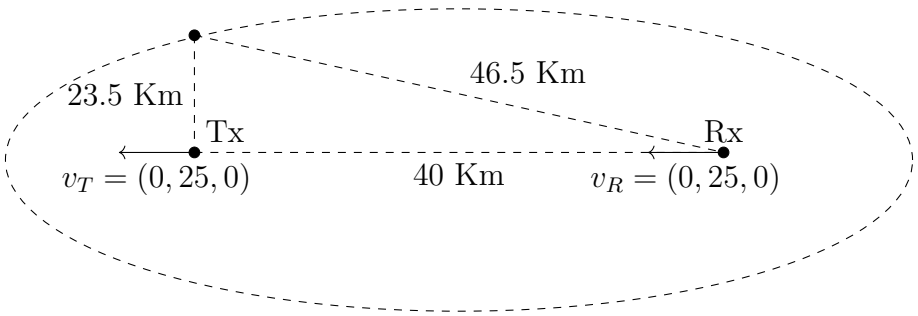

Figure 8: Scenario

	Scenario			
Radar Parameter	**5**	**6**	**7**	**8**
Antenna peak gain in Tx	12 dB	12 dB	12 dB	12 dB
Number of Tx channels	16	16	16	16
Number of Rx channels	20	20	20	20
Number of pulses	20	20	20	20
Antenna gain in receiver	0 dB	0 dB	0 dB	0 dB
Antenna element spacing	0.025 m	0.025 m	0.025 m	0.025 m
Pulse repetition frequency	1400 Hz	2100 Hz	2100 Hz	2100 Hz
Wavelength	0.05 m	0.05 m	0.05 m	0.05 m
Thermal noise power in Rx	-170 dB	-130 dB	-130 dB	-130 dB
Transmitter's speed ($\|v_T\|$)	25 m/s	25 m/s	25 m/s	25 m/s
Receiver's speed ($\|v_R\|$)	25 m/s	25 m/s	25 m/s	25 m/s
Heading angle difference	45°	45°	90°	180°
Distance between platforms	40 Km	40 Km	40 Km	40 Km

Table 2: Radar parameters for scenarios 5 to 8

4.1 Inhomogenous Background Effect

In this part effect of inhomogenous clutter reflectivity against a homogeneous background is demonstrated using the first scenario in Table 1. To further see this effect, both transmitter and receiver are located at one point creating a monostatic configuration so that the complexity of bistatic scenario is removed from the picture. Also, number of transmitter antenna elements is set to 1 so that all areas are illuminated with the same amount of power. The distance to the range bin is also selected to be 70 Km.

A SINR plot typically visualizes the equation 2.15 across a range of angles and Doppler frequencies, displaying how the SINR varies with changes in the direction and relative velocity (Doppler shift) of the target signal. In the SINR plot in Figure 9, there is a ridge which indicates the clutter effect and has lower SINR value compared to other parts that are noise limited area. The right figure is for the homogeneous background and the clutter ridge is symmetric with the highest value at Doppler frequency of 0 and this value falls off gradually to both sides of it. This means that its hard for a stationary target that has 0 Doppler to be distinguished from clutter. The left figure shows the SINR plot for inhomogenous background type II. The clutter ridge is no longer symmetric and the part with the lowest SINR corresponds to the patches with highest reflectivity coefficients.

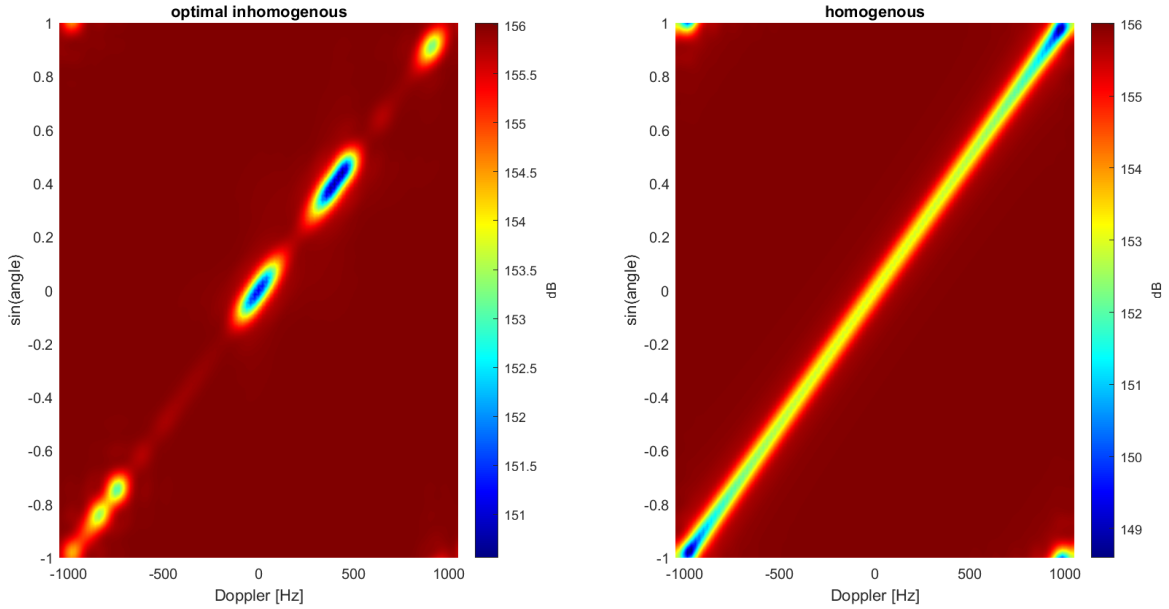

Figure 9: SINR for monostatic setup

4.2 PRF Impact

When the relative speed between a scatterer and both radar platforms is high enough for the Doppler frequency to exceed PRF, then radial velocity aliasing occurs. The lowest PRF that gives unambiguous frequency is given by the expression:

$$\text{PRF} = 2(\frac{v_t}{\lambda}\mathbf{d}_{Tx}^T\mathbf{d}_{TxP_s} + \frac{v_r}{\lambda}\mathbf{d}_{Rx}^T\mathbf{d}_{RxP_s}) \tag{4.1}$$

In this setup, we use the second and third scenarios from Table 1. In the setup shown in Figure 8, both platforms move in one direction and have the same speed of 25 m/s, resulting in a minimum PRF of 2 kHz. In Figure 10, two SINR plots are displayed: one for the low PRF of 1.4 kHz (second scenario) which introduces aliasing, and another for the higher PRF of 2.1 kHz (third scenario). This demonstrates the effects of aliasing due to the insufficient PRF in the second scenario.

4.3 Detector Comparison

In this section, detectors' performances are compared to one another. To this end, the third scenario from Table 1 is used and 20 different background realizations are drawn for each of background types I and II. Figures 11 and 13 show the KLD distance between covariance matrices of optimal detector with both suboptimal and subspace 2 detector for these 20 background realizations. In these figure the background type I and II are implemented respectively. One way to measure the performance of a detector is to see how much clutter is mitigated; meaning how many point in SINR plot are noise

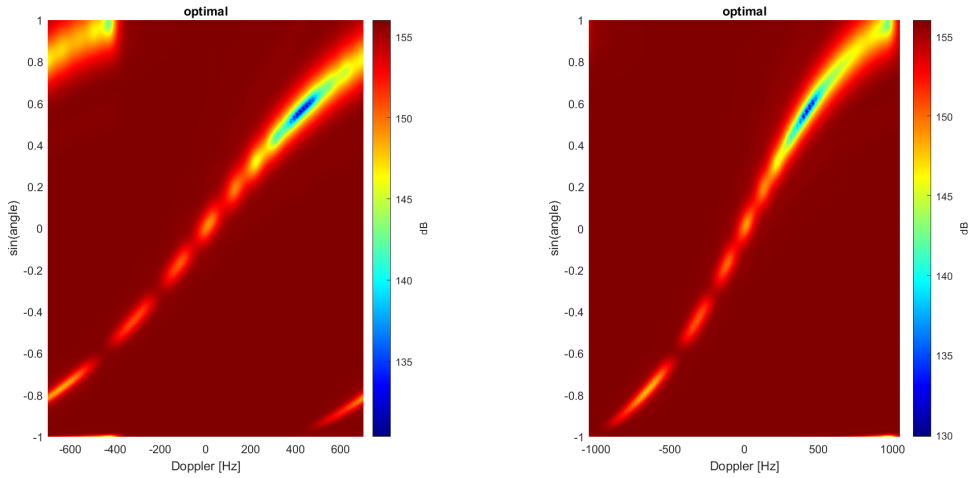

(a) PRF=1400 Hz (b) PRF=2100 Hz

Figure 10: SINR plot for different PRF values

limited and how wider the clutter ridge is. We define a region as clutter limited when its SINR value is 6 dB less than the maximum SINR value in that scenario. Larger area of clutter regions means the detector has a worse performs.

Figures 12 and 14 shows the ratio of clutter limited regions to the whole area. For the type I background, KLD distance of suboptimal for all realizations is less than the subspace 2 suggesting that in this smooth changing background, suboptimal performs better. This is verified in Figure 12. After optimal detector which has the best performance amongst all, suboptimal comes next for all 20 cases. However in background type II this is not certain as shown in Figure 13, the KLD distance fluctuates depending on the realization. When the KLD distance for either of these two detectors becomes less, the performance of that detector surpasses the other one for that realization in Figure 14. For both background types, it is worth noting that subspace 1 showed the poorest performance.

Figure 15 and 16 shows the SINR plots for different detectors for realization number 15. For this realization, subspace 2 has a higher performance than the suboptimal detector as clutter ridge has a higher SINR value. Figure 17 shows the ratio of subspace 2 SINR to suboptimal one in dB which shows subspace 2 has a performance that is up to 18 dB higher than suboptimal. As mentioned in previous section, the reason for this difference is that in case the assumed homogeneous background has a higher clutter power than what is in the real case scenario, detector removes more power from the received signal than it should. This causes the useful information to be lost and causes a degraded performance. The clutter power that detector removes from the signal is defined by $\boldsymbol{s}_{st}^H \hat{\boldsymbol{R}}_k \boldsymbol{s}_{st}$. The right plot in Figure 17 shows the ratio of this clutter power in homogeneous case to the inhomogenous background which proves this point. Figure 18

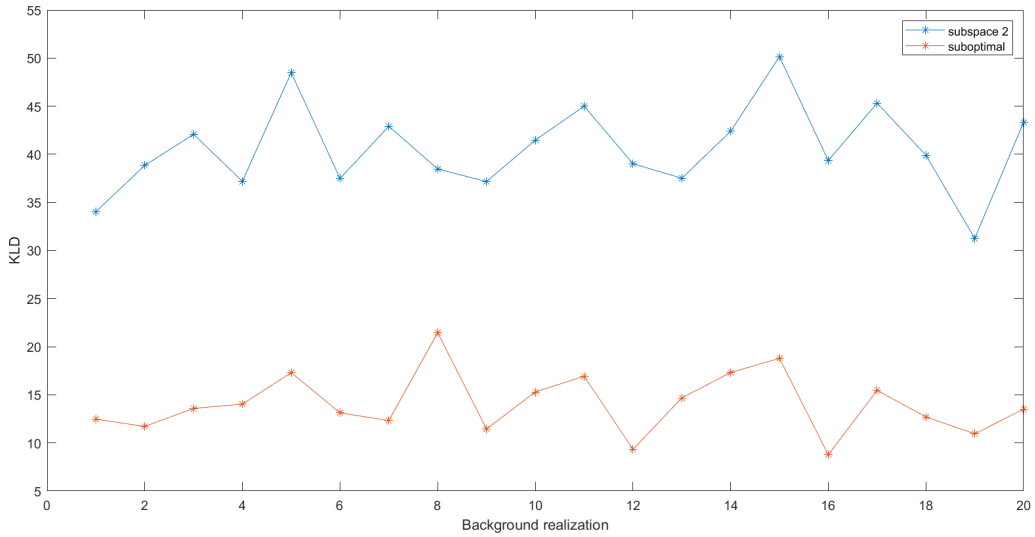

Figure 11: KLD for background type I

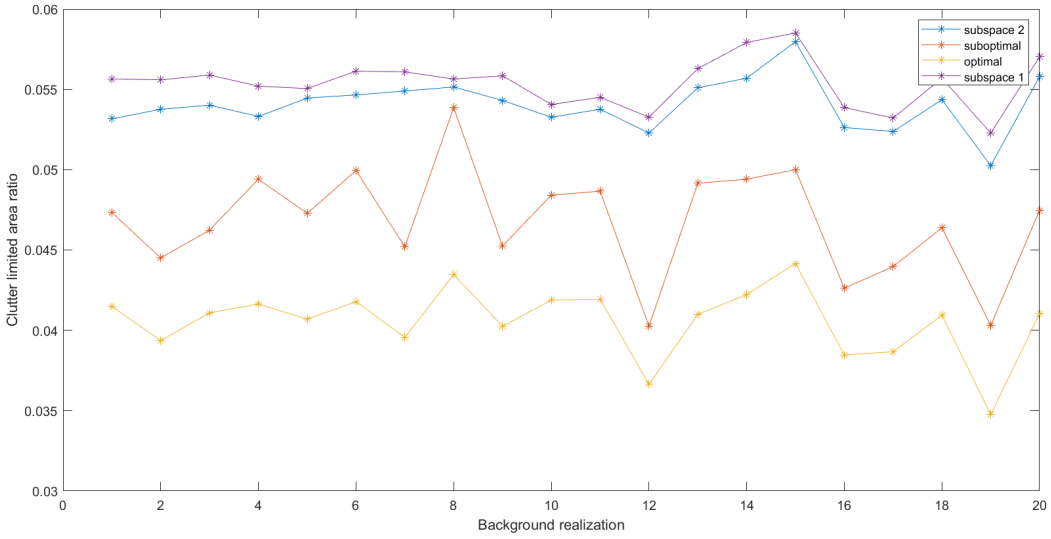

Figure 12: Clutter limited area ratio for background type I

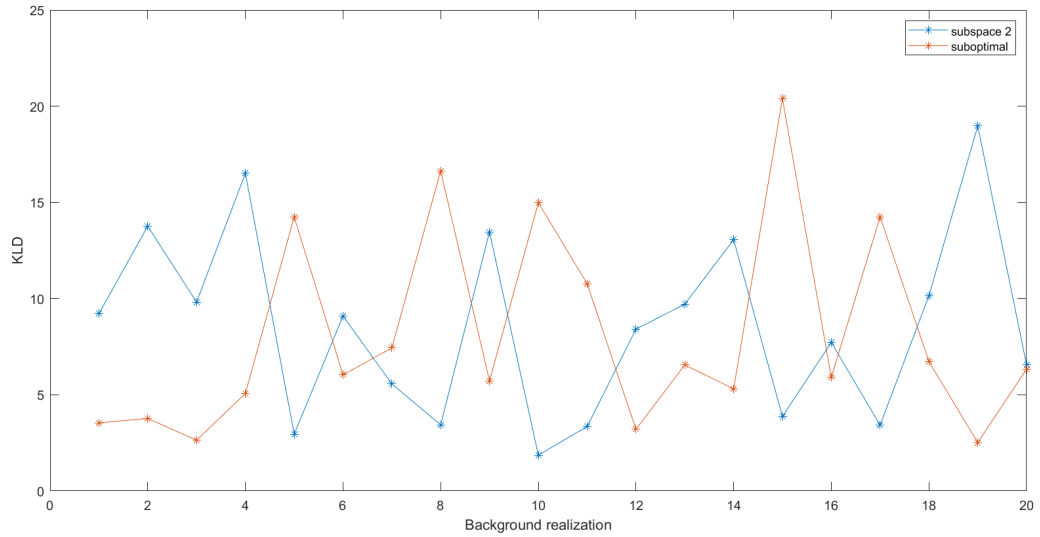

Figure 13: KLD for background type II

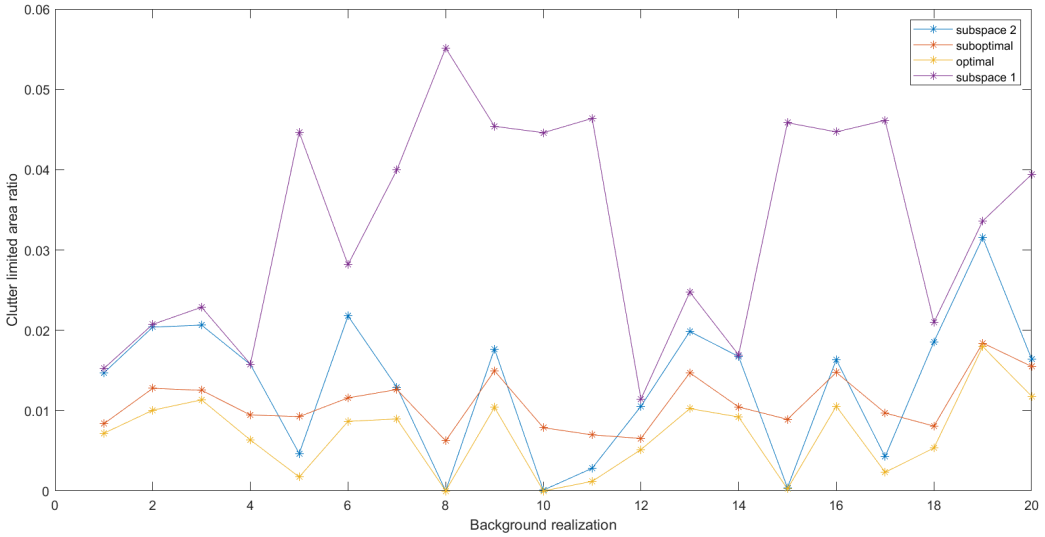

Figure 14: Clutter limited area ratio for background type II

and 19 shows the corresponding plots for realization 1 which gives a better performance for suboptimal detector.

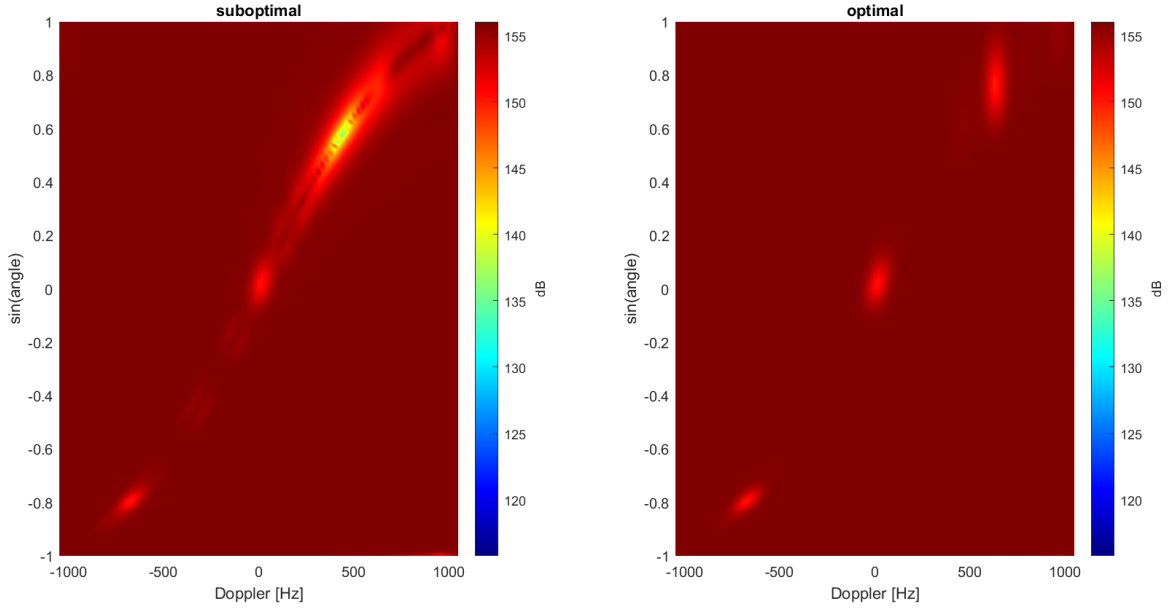

Figure 15: SINR for realization 15

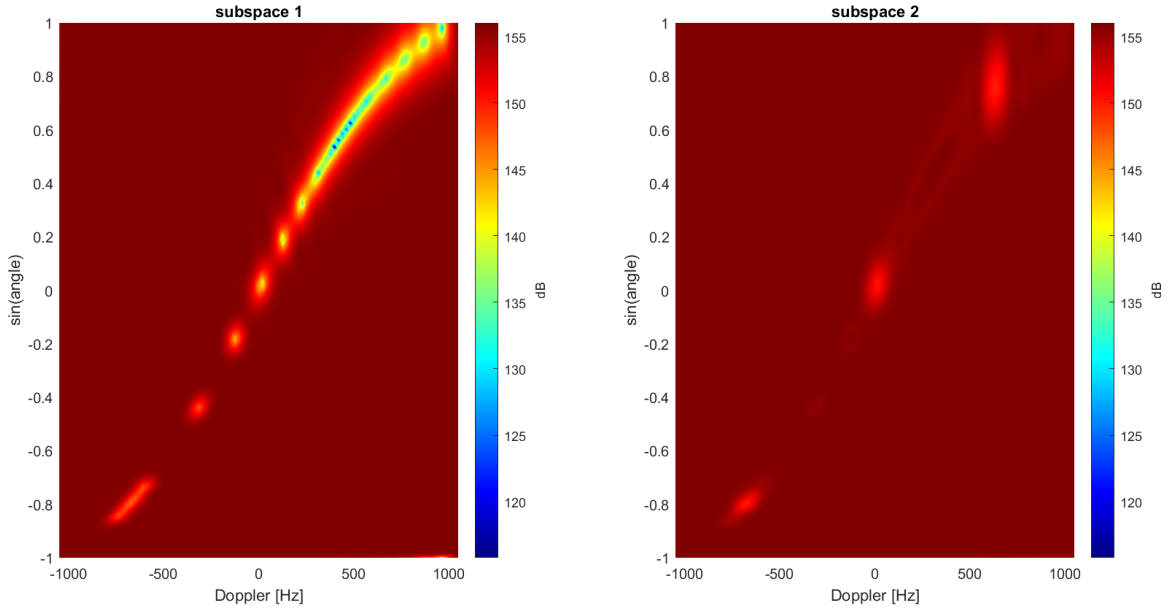

Figure 16: SINR for realization 15

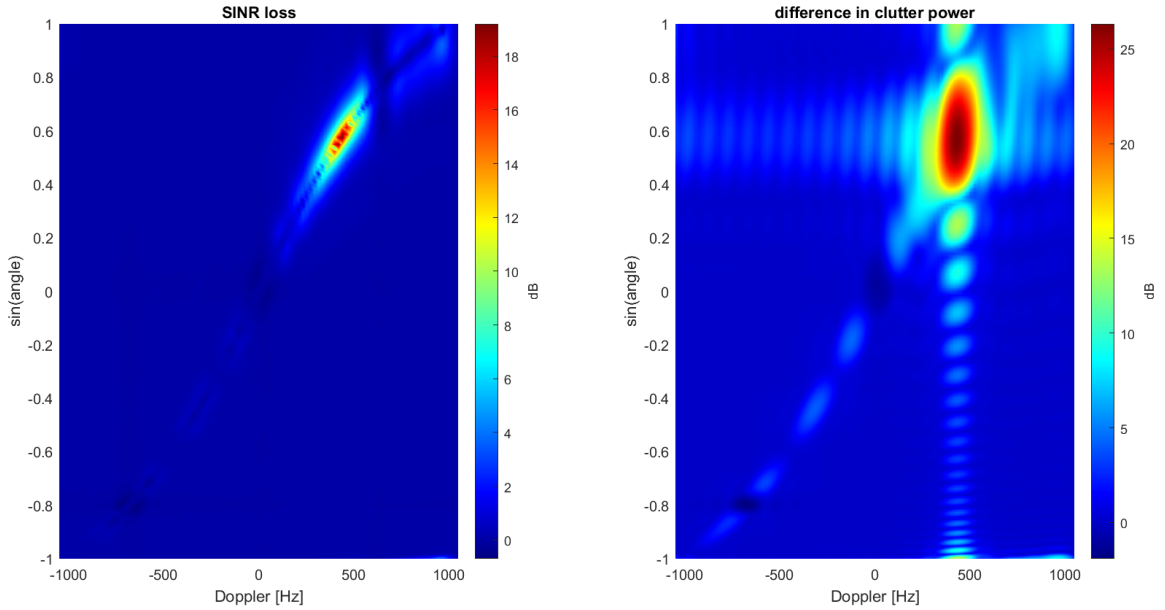

Figure 17: SINR loss and clutter power for realization 15

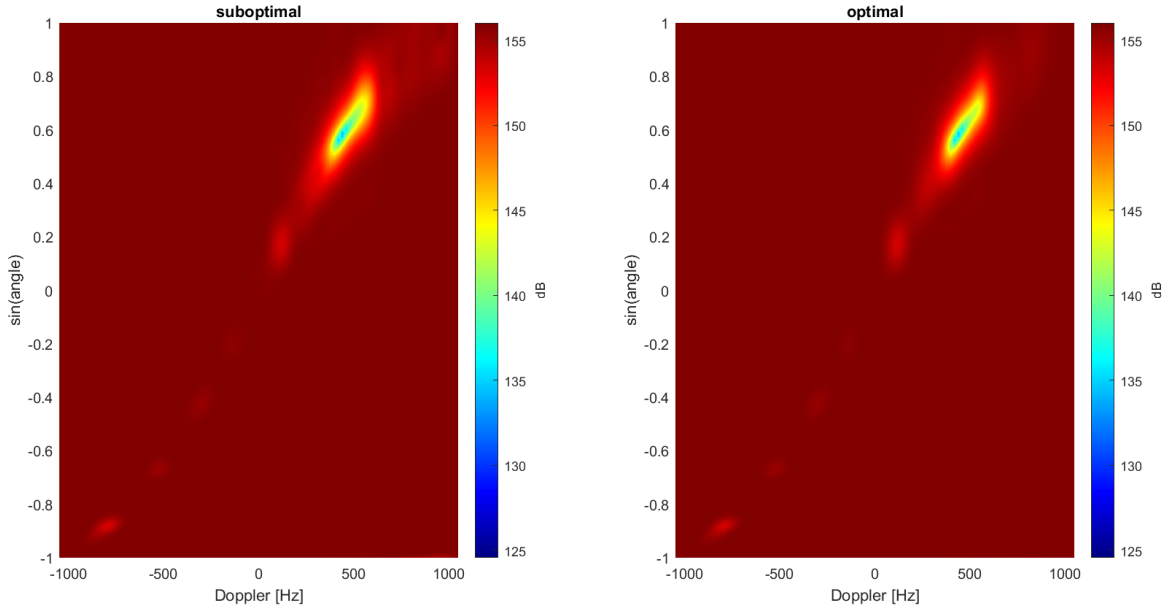

Figure 18: SINR for realization 1

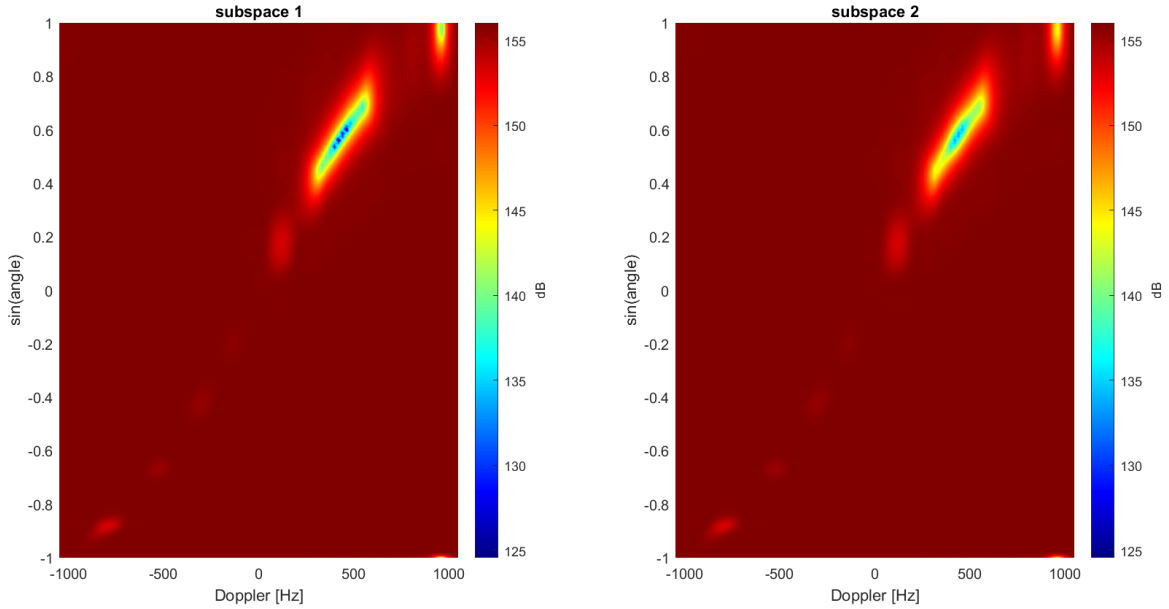

Figure 19: SINR for realization 1

4.4 Noise Level Impact

In this section, the effect of the thermal noise is investigated. For this part, the 4^{th} scenario in Table 1 and 5^{th} scenario in Table 2 are implemented. In these scenarios, the PRF is 14 KHz and the range bin is selected to be 60 Km. In this simulation the background type II with the correlation length of 20 Km is implemented. Platforms are moving with 45° difference in their heading direction. It should be noted that in this simulation, there has been no scaling on returned clutter power, however the homogeneous clutter reflectivity is selected so that is it equivalent to the average of all reflectivity values in all realizations.

Theoretically, when decreasing thermal noise level, it is expected to see the effect of different background realizations more distinctly because the effect of clutter becomes more dominant. Figure 20 and 21 display SINR values for radial velocity of 420Hz across multiple background realizations, comparing optimal and suboptimal detectors under different levels of thermal noise power. Comparing the SINR plots for different detector types, it can be seen that optimal detector follows this expectation. However, contrary to expectations, curves corresponding to suboptimal detector becomes more similar when the noise level is decreased.

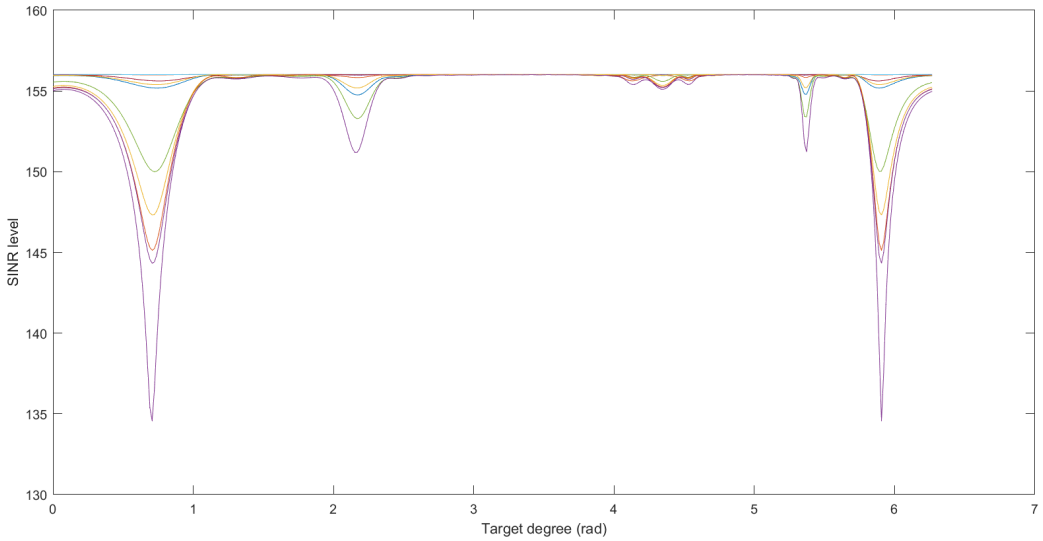

(a) $\sigma_n^2 = 10^{-13}$

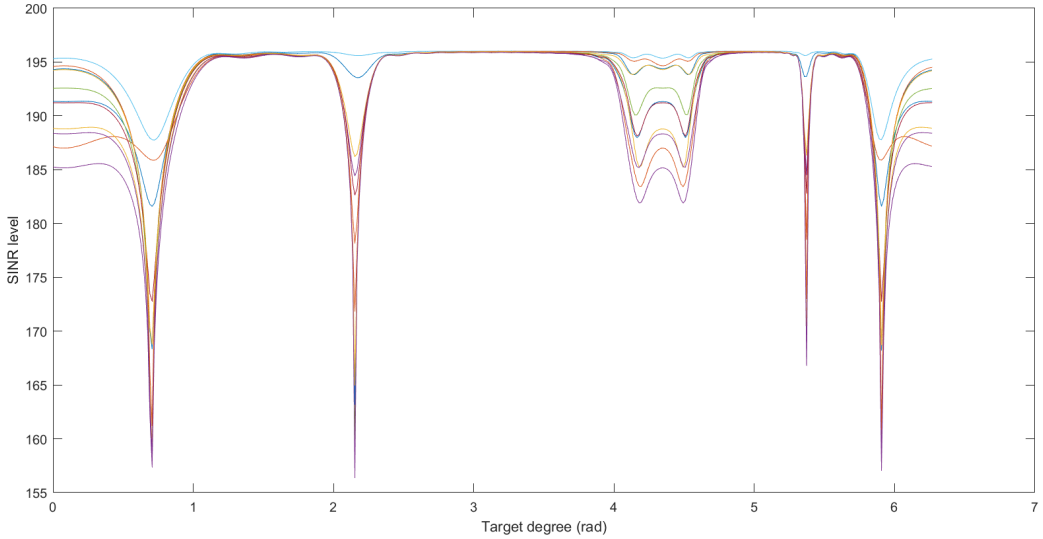

(b) $\sigma_n^2 = 10^{-17}$

Figure 20: Optimal detector SINR results for various noise levels

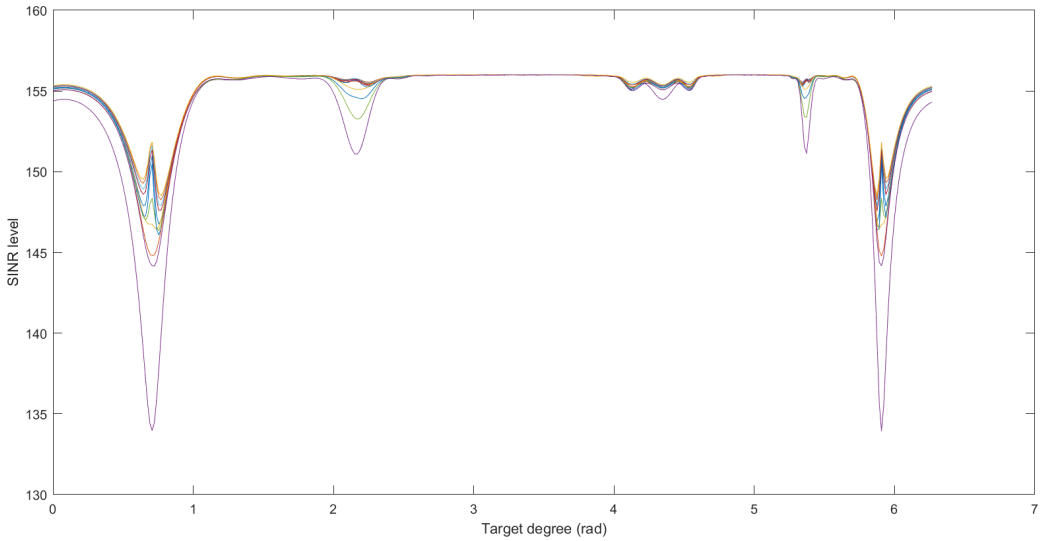

(a) $\sigma_n^2 = 10^{-13}$

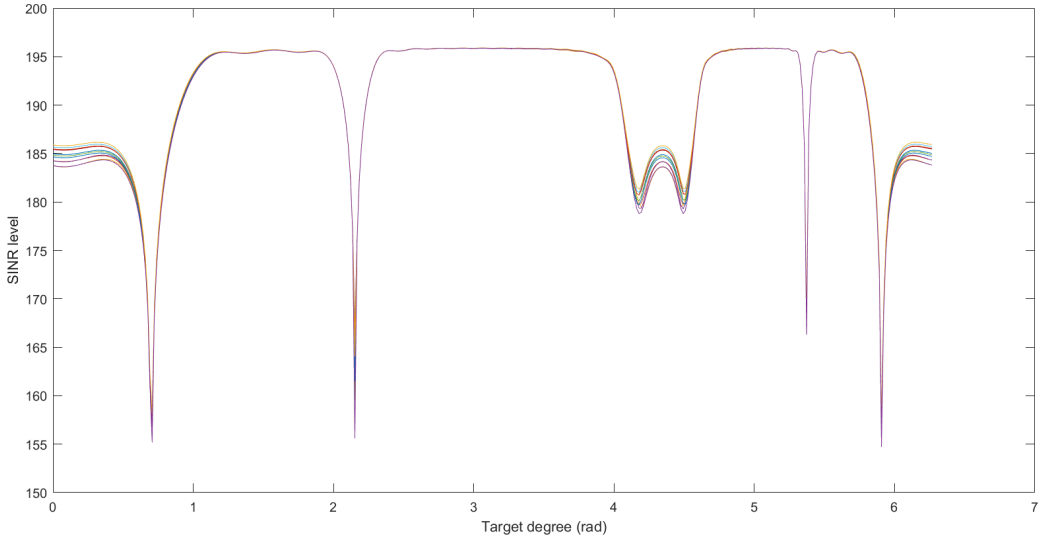

(b) $\sigma_n^2 = 10^{-17}$

Figure 21: Suboptimal detector SINR results for various noise levels

4.5 Maximum Likelihood Estimation Results

As mentioned before, due to separate locations of the two platforms, receiver has no information about transmitter parameters. This information is crucial in order to estimate the covariance matrix accurately. To this end, receiver needs to estimate these parameters from secondary data. In this section the numerical simulation for estimating transmitter parameters is performed. The estimated parameters are $\boldsymbol{\xi} = [x_T, y_T, z_T, |v_T|, \varphi_{vt}, \theta_0]$. For this simulation, the third scenario from Table 1 is implemented and it is assumed that transmitter moves parallel to the ground meaning that $\theta_{vt} = \pi/2$ and it is known to the receiver. In this scenario transmitter and receiver have the same velocity vector of (0,25,0) m/s. Tx and Rx are located at the coordinate (0,20,4) Km and (0,-20,4) Km respectively. The transmitter's main lobe is illuminating the broadside of the antenna which makes $\theta_0 = \pi/2$. The initial value vector, $\boldsymbol{\xi}_0$ is defined at the true values for all parameters. This is carried out to solely observe the error caused by the inhomogeneity. In the expression defined at (3.20), the secondary data, $\boldsymbol{r}_k$, come from the inhomogenous background, from 10 range bins located between 45 Km and 100 Km. However, since the real background is not known to the processor, it assumes a homogeneous clutter reflectivity in the model for $\boldsymbol{R}_k$.

To ensure minimize errors arising from different scales, all these parameters are normalized within the range of 0 to 1 based on their respective predefined operational limits. This normalization involves dividing each parameter by a number that represents its maximum possible value, followed by an offset adjustment where needed. The simulation is repeated 20 times for Monte Carlo analysis with each Monte Carlo iteration resulting in six normalized estimated parameters. Afterwards, for each iteration, the root mean square error (RMSE) for these six parameters are calculated collectively, giving a single RMSE value that is the representative of the estimation accuracy. Figure 22 represents the box plot for a few realizations in both background types against different correlation lengths. Additionally, Figure 23 represents the combined RMSE value, calculated from the RMSEs of all 20 Monte Carlo runs against different correlation lengths. Although it was expected to have a lower RMSE for extremely low and high correlation lengths, these two plots show a different outcome. This expectation is because an extremely low correlation length results in randomness, while a high correlation length tends to make the background more homogeneous.

Another experiment is done for varying angles of heading between the transmitter and receiver, where both platforms move with a specific angle between them, which are the third, 6^{th}, 7^{th} and 8^{th} scenarios defined in Table 1 and 2. All the scenario specifications including the absolute speed are the same except the angle of heading. Figure 24 shows these results in a box plot. It can be seen that the parameters are estimated more accurately for higher angle between platforms until 90°.

Additionally, in Figures 25 to 29, the log likelihood function is plotted as a function of

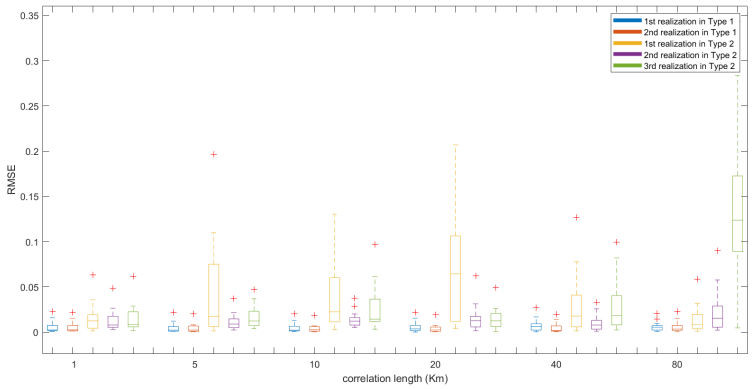

Figure 22: Box plot for RMSE values over 20 iterations for different correlation lengths

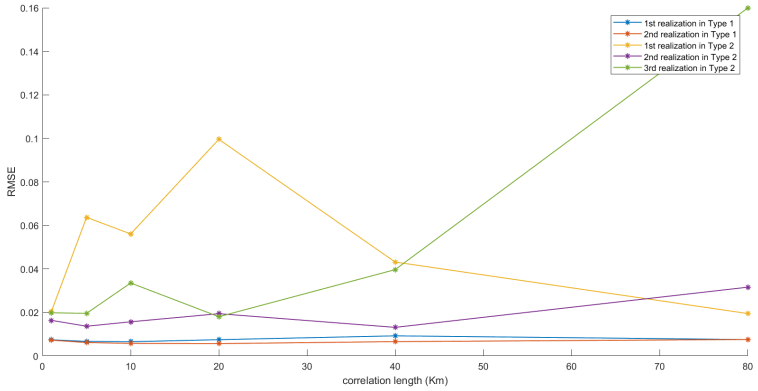

Figure 23: Combined RMSE from 20 Monte Carlo simulations over different correlation lengths

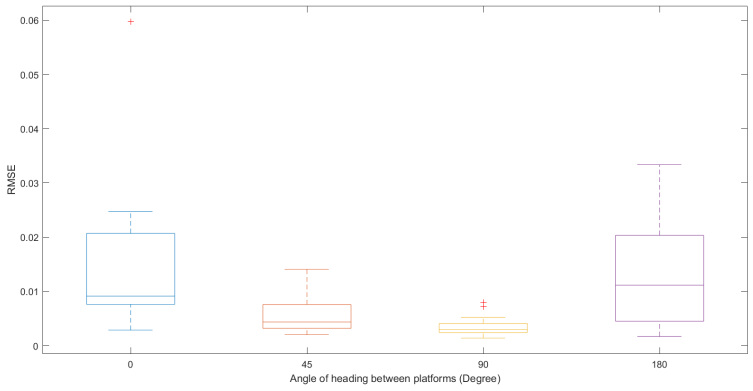

Figure 24: Impact of varying heading angle on system performance

each parameter for both homogeneous and inhomogenous backgrounds using the third scenario in Table 1. Each of these curves in these plots correspond to a certain number of rage bins (between 45 and 71 Km) used in (3.20). In order to plot several data curves in one figure for each parameter, these curves are scaled based on the number of range bins. Moreover, for one of the data curves, it is assumed that the true covariance matrix $\boldsymbol{R}_0$ is available and used in the log-likelihood calculations instead of the secondary data. This is reflected in the modified log-likelihood equation:

$$\hat{\boldsymbol{\xi}} = \arg\min_{\boldsymbol{\xi}} \ln L(\boldsymbol{\xi}|\mathbf{r}) = \sum_{k=1}^{K} \left(\ln \left(\det(\boldsymbol{R}_k(\boldsymbol{\xi})) \right) + \operatorname{trace}(\boldsymbol{R}_0 \boldsymbol{R}_k^{-1}(\boldsymbol{\xi})) \right) \tag{4.2}$$

For each transmitter parameter, this curve is also plotted to show the behavior of the function, highlighting the performance when the true covariance matrix $\boldsymbol{R}_0$ is used in the calculations.

These figures show that, in most cases, increasing the amount of secondary data improves the accuracy of parameter estimation. It is because when using data from more range bins, the increased diversity in data provides more information, resulting in a less flat ML curve. As expected, the absolute minimum for curves corresponding to the inhomogenous background don't always match the true values. Moreover, for this background, there are more notches and these local minimums make the choice of initial values more tricky as it may cause the algorithm to converge to the local optimal value instead of the global one.

Looking at Figure 25, we observe that the curves have sharp changes at certain values. However, the curves should change smoothly; a slight change in the value should result in a corresponding slight change in the log-likelihood function. When we repeat the same plotting for the 6^{th} scenario that has a receiver moving at 45° angle difference compared to the transmitter, this sharp changes does not occur as can be seen in Figure 30. This suggest that this error happens due to numerical inaccuracies caused by MATLAB and is scenario related. Additionally, it is important to note the different scales in the log-likelihood plots as well. When both platforms are moving in the same direction, estimating transmitter position on x happen to be symmetric relative to its angle of heading. However, it should be noted that such a scenario is unlikely to happen in the real world.

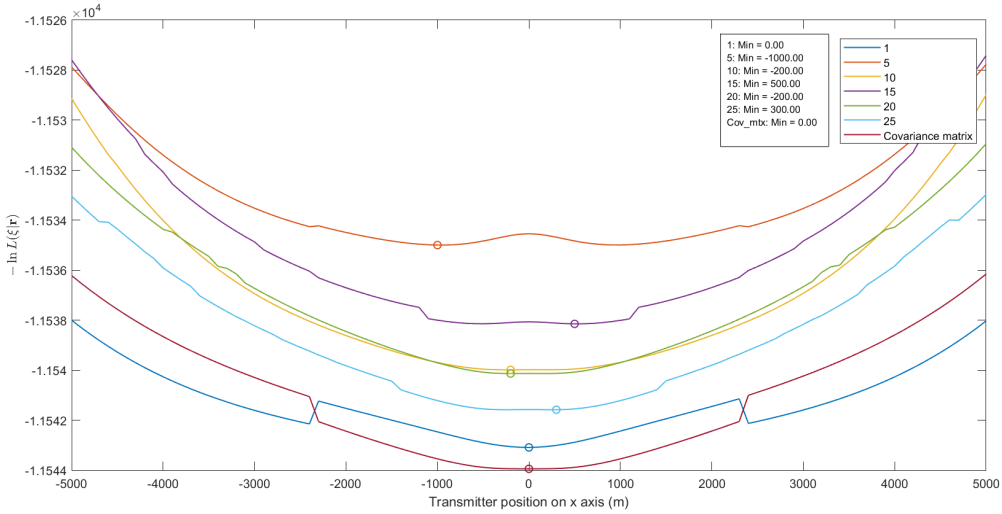

(a) Homogeneous

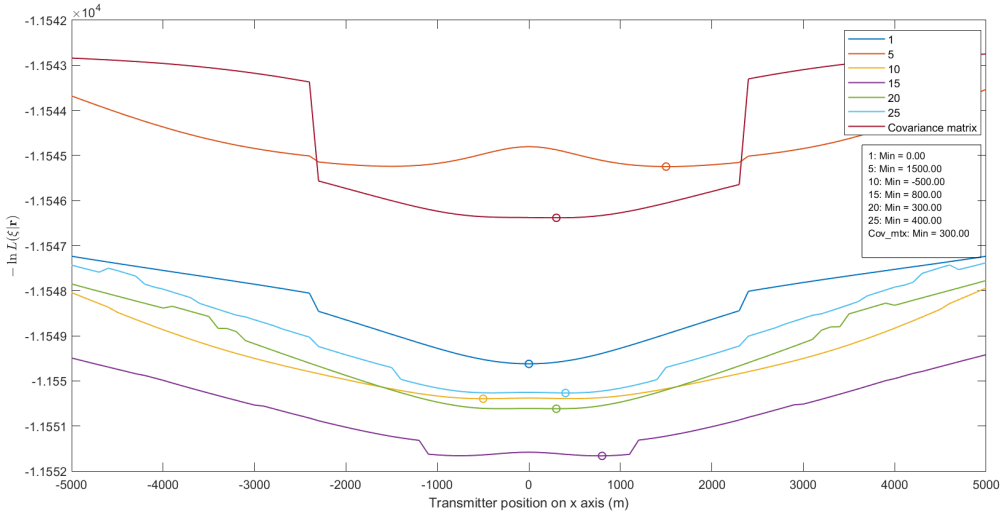

(b) Inhomogenous

Figure 25: Log-likelihood as a function of transmitter position on x axis for both homogeneous and inhomogenous backgrounds with the true value of x being at 0 m

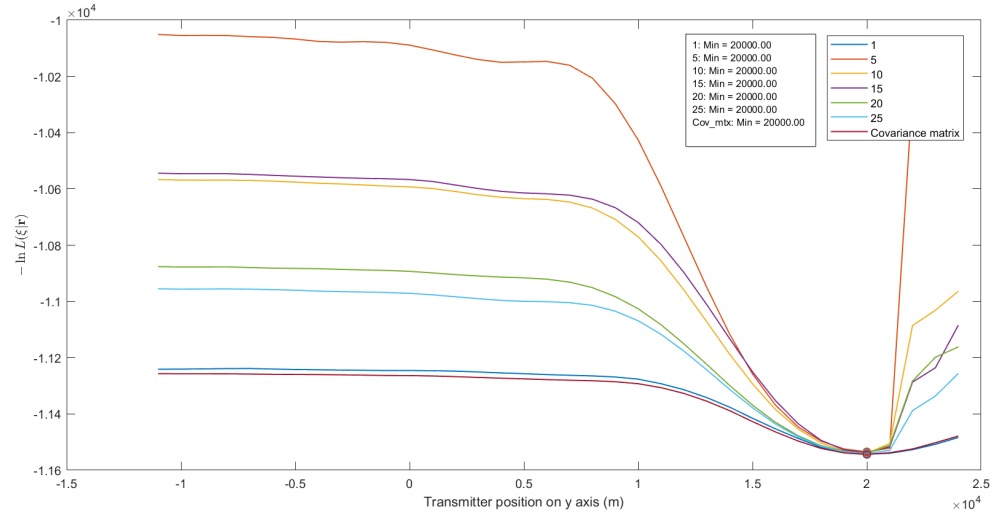

(a) Homogeneous

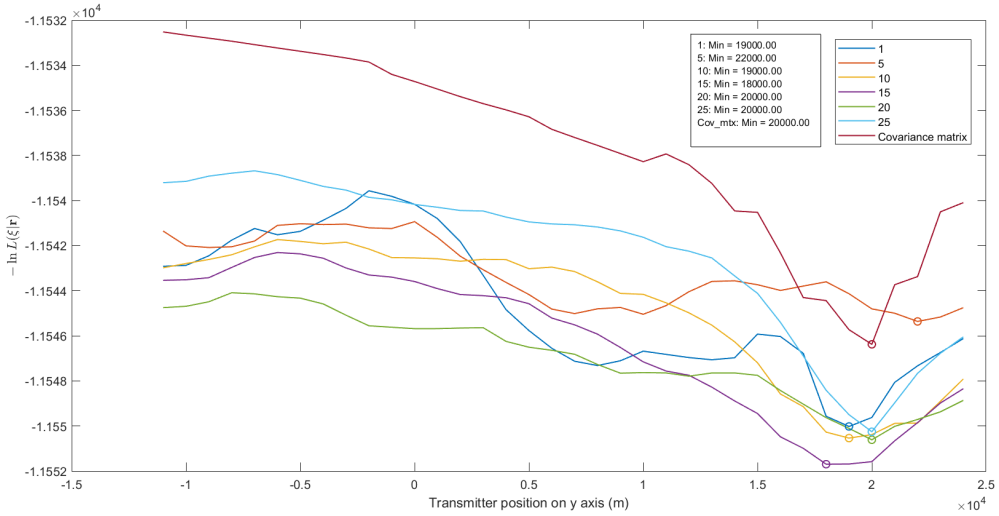

(b) Inhomogenous

Figure 26: Log-likelihood as a function of transmitter position on y axis for both homogeneous and inhomogenous backgrounds with the true value of y being at 20 Km

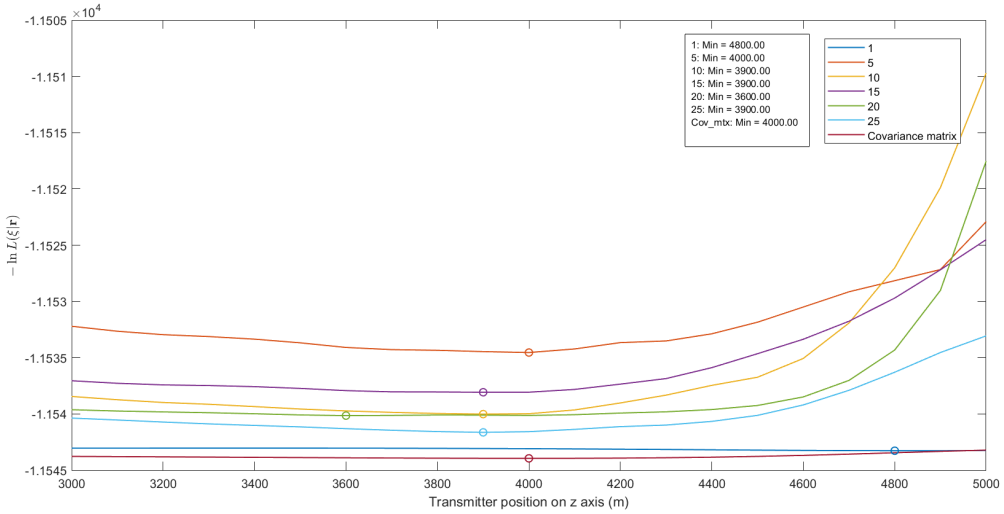

(a) Homogeneous

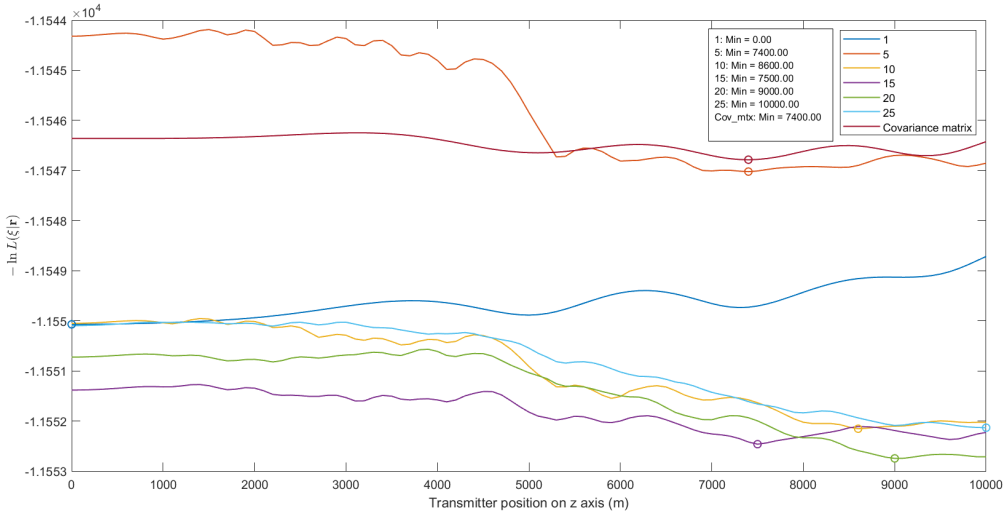

(b) Inhomogenous

Figure 27: Log-likelihood as a function of transmitter position on z axis for both homogeneous and inhomogenous backgrounds with the true value of z being at 4 Km

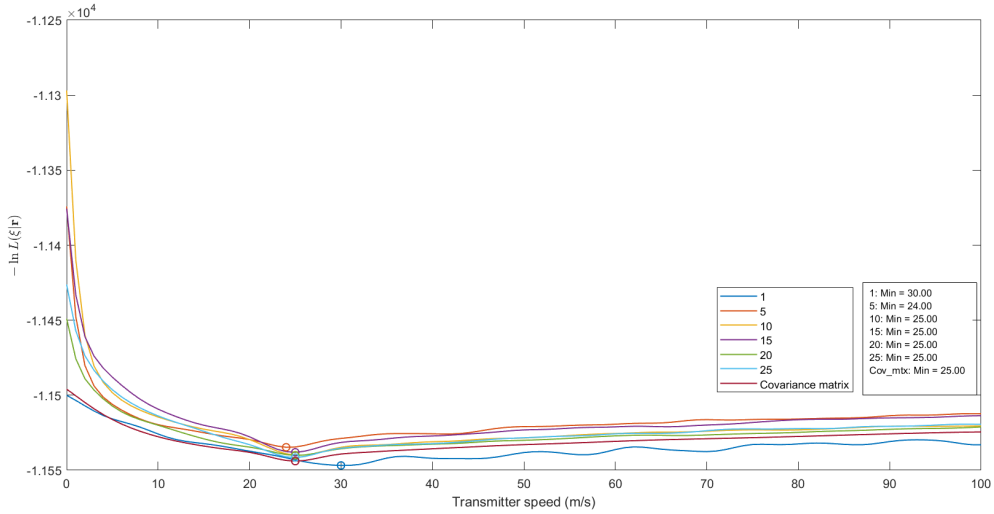

(a) Homogeneous

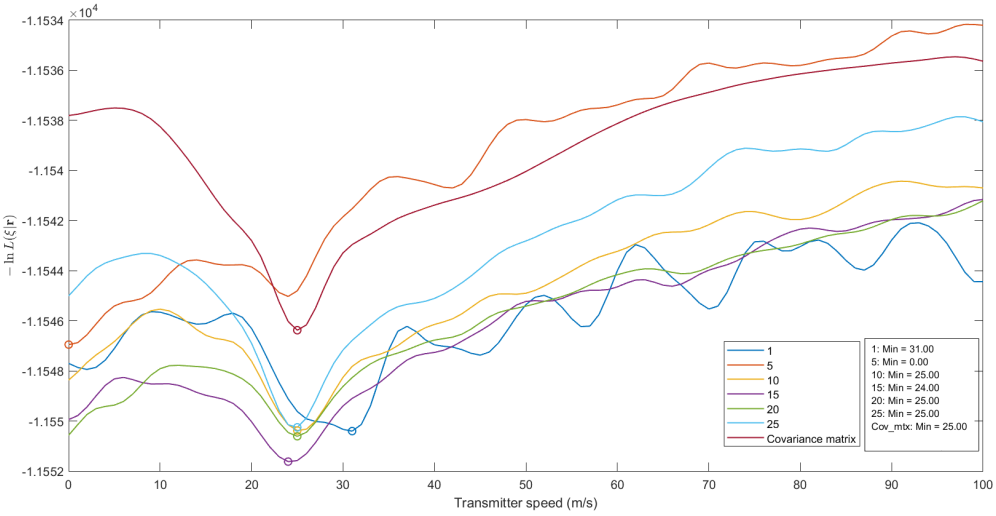

(b) Inhomogenous

Figure 28: Log-likelihood as a function of transmitter speed for both homogeneous and inhomogenous backgrounds with the true value of speed being at 25 m/s

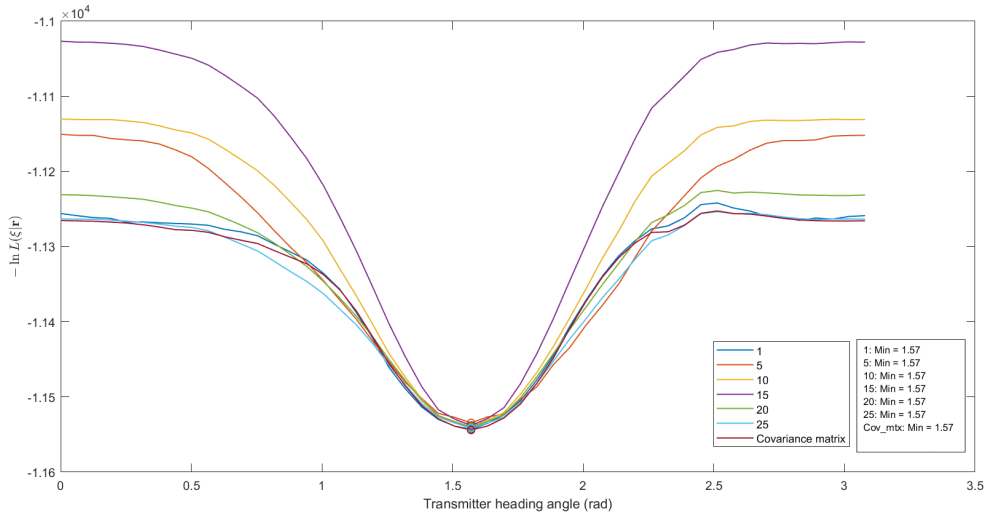

(a) Homogeneous

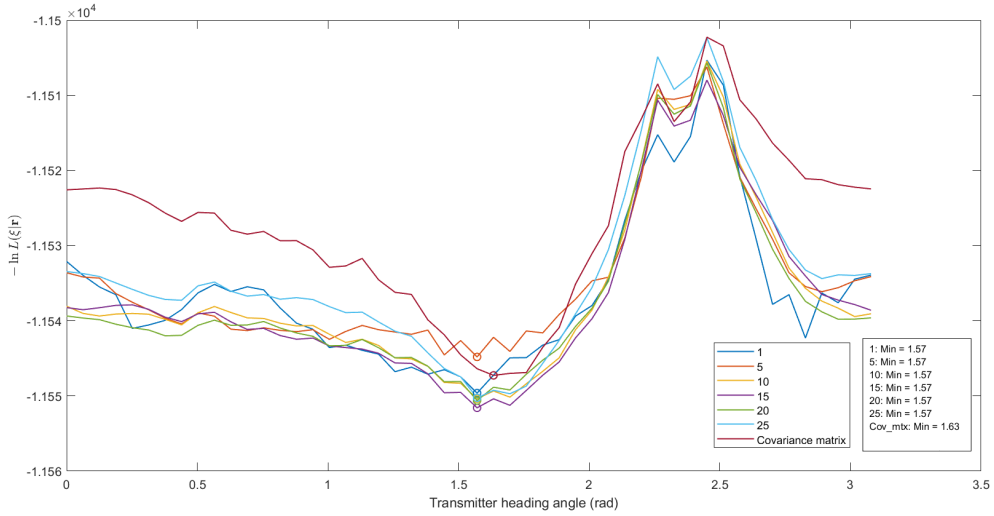

(b) Inhomogenous

Figure 29: Log-likelihood as a function of transmitter heading direction for both homogeneous and inhomogenous backgrounds with the true value of direction being at $\pi/2$ rad

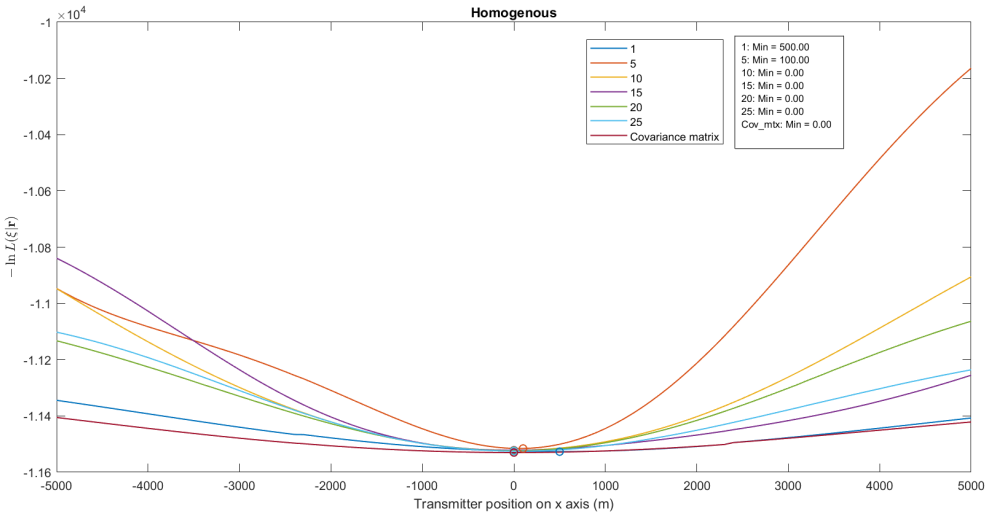

Figure 30: Log-likelihood as a function of transmitter position on x axis for both homogeneous background, considering the receiver moves at an angle to the transmitter with the true value of x being at 0 m

5

Conclusion

In this thesis we began by developing a model for background reflectivity coefficients to evaluate airborne bistatic radar performance in inhomogenous environment. Afterwards, different detectors are tested against this setup and theirs performance is compared with that of homogeneous background. The detectors tested include optimal, suboptimal, and subspace detectors. The optimal detector assumes full access to the true covariance matrix, while the suboptimal detector involves fitting the homogeneous covariance matrix to the inhomogeneous one. The subspace detector, on the other hand, removes certain directions with the most disturbance from the signal, leaving the directions where thermal noise plays a larger role compared to clutter unaffected.

Looking at the results, we can see that as expected optimal detector performs the best regardless of the scenario and background. For the suboptimal detectors, their performance varies: in some background realizations, the subspace detector performs better, while in others, the suboptimal detector shows higher performance. Following this, we attempted to estimate transmitter parameters using the secondary data with the log-likelihood function. It can be concluded that in a homogeneous background, there is greater flexibility in choosing initial values for the parameters to be estimated, with a relatively wide range leading to the maximum likelihood estimate converging to the global maximum. However, in inhomogenous background, there is a greater possibility for the ML function to converge to the local maxima.

For the future work, in the tracking problem, it is important to use data from the range bins that causes the ML function to converge to the true value. This must be done by actively selecting range bins with higher clutter power. Moreover, the distance of the selected range bins can impact the efficiency of this algorithm. It is essential to investigate whether using range bins at greater or shorter distances yields better results.

References

[1] M. Skolnik, "Fifty years of radar," *Proceedings of the IEEE*, **jourvol** 73, **number** 2, **pages** 182–197, 1985. DOI: 10.1109/PROC.1985.13132.

[2] R. M. Page, "The early history of radar," *Proceedings of the IRE*, **jourvol** 50, **number** 5, **pages** 1232–1236, 1962. DOI: 10.1109/JRPROC.1962.288078.

[3] I. Bilik, "Comparative analysis of radar and lidar technologies for automotive applications," *IEEE Intelligent Transportation Systems Magazine*, **jourvol** 15, **number** 1, **pages** 244–269, 2023. DOI: 10.1109/MITS.2022.3162886.

[4] H. Griffiths, "From a different perspective: Principles, practice and potential of bistatic radar," *2003 Proceedings of the International Conference on Radar (IEEE Cat. No.03EX695)*, **pages** 1–7, 2003. DOI: 10.1109/RADAR.2003.1278701.

[5] R. Duan, X. Wang **and** Z. Chen, "Space-time clutter model for airborne bistatic radar with non-gaussian statistics," **in***2008 IEEE Radar Conference* 2008, **pages** 1–6. DOI: 10.1109/RADAR.2008.4720814.

[6] W. Melvin, "Space-time adaptive radar performance in heterogeneous clutter," *IEEE Transactions on Aerospace and Electronic Systems*, **jourvol** 36, **number** 2, **pages** 621–633, 2000. DOI: 10.1109/7.845251.

[7] X. Wang, E. Aboutanios **and** M. G. Amin, "Slow radar target detection in heterogeneous clutter using thinned space-time adaptive processing," *IET Radar, Sonar & Amp; Navigation*, **jourvol** 10, **pages** 726–734, 4 2016. DOI: 10.1049/iet-rsn.2015.0307.

[8] S. Bidon, O. Besson **and** J.-Y. Tourneret, "Knowledge-aided STAP in heterogeneous clutter using a hierarchical bayesian algorithm," *IEEE Transactions on Aerospace and Electronic Systems*, **jourvol** 47, **number** 3, **pages** 1863–1879, **july** 2011. DOI: 10.1109/TAES.2011.5937270. **url**: https://hal.science/hal-03610420.

[9] W. Melvin **and** G. Showman, "An approach to knowledge-aided covariance estimation," *IEEE Transactions on Aerospace and Electronic Systems*, **jourvol** 42, **number** 3, **pages** 1021–1042, 2006. DOI: 10.1109/TAES.2006.248216.

[10] M. I. Skolnik, *Radar handbook second edition*. McGrawHill, 1990.

[11] W.Melvin, *Space-time detection theory, Military Application of Space Time Adaptive Processing*. 2003.

[12] D. MacKay, *Information Theory, Inference and Learning Algorithms*. Cambridge University Press, 2003, ISBN: 9780521642989. **url**: https://books.google.se/books?id=AKuMj4PN_EMC.

[13] T. McKelvey, "Kullback-leibler divergence for circular symmetric complex gaussian distributions," *Internal document*, 2024.

[14] T. McKelvey, "Bistatic clutter modelling," *Internal document*, 2023.

[15] J. Billingsley, A. Farina, F. Gini, M. Greco **and** L. Verrazzani, "Statistical analyses of measured radar ground clutter data," *IEEE Transactions on Aerospace and Electronic Systems*, **jourvol** 35, **number** 2, **pages** 579–593, 1999. DOI: 10.1109/7.766939.

[16] J. Klintberg, T. McKelvey **and** P. Dammert, "A parametric approach to space-time adaptive processing in bistatic radar systems," *IEEE Transactions on Aerospace and Electronic Systems*, **jourvol** 58, **number** 2, **pages** 1149–1160, 2022. DOI: 10.1109/TAES.2021.3122520.

DEPARTMENT OF ELECTRICAL ENGINEERING
CHALMERS UNIVERSITY OF TECHNOLOGY
Gothenburg, Sweden
www.chalmers.se

CHALMERS
UNIVERSITY OF TECHNOLOGY